Ministério da
Ciência e Tecnologia

INPE-XXXX-XXX/XX - versão X

SIGNATURES OF TWO DISTINCT DRIVING MECHANISMS IN THE EVOLUTION OF CORONAL MASS EJECTIONS IN THE LOWER CORONA.

Cristiane Loesch de Souza Costa

Tese de Doutorado em Geofísica Espacial, orientada pela Prof. Dr. Maria Virginia Alves e pela Prof. Dr. Merav Opher, aprovada em 03 de abril de 2009.

Original document registry:
<http://urlib.net/XXXcolocarXXX>

INPE
São José dos Campos
2009

PUBLICADO POR:

Instituto Nacional de Pesquisas Espaciais - INPE
Gabinete do Diretor (GB)
Serviço de Informação e Documentação (SID)
Caixa Postal 515 - CEP 12.245-970
São José dos Campos - SP - Brasil
Tel.:(012) 3945-6911/6923
Fax: (012) 3945-6919
E-mail: pubtc@sid.inpe.br

Ministério da
Ciência e Tecnologia

INPE-XXXX-XXX/XX - versão X

SIGNATURES OF TWO DISTINCT DRIVING MECHANISMS IN THE EVOLUTION OF CORONAL MASS EJECTIONS IN THE LOWER CORONA.

Cristiane Loesch de Souza Costa

Tese de Doutorado em Geofísica Espacial, orientada pela Prof. Dr. Maria Virginia Alves e pela Prof. Dr. Merav Opher, aprovada em 03 de abril de 2009.

Original document registry:
<http://urlib.net/XXXcolocarXXX>

INPE
São José dos Campos
2009

Cataloging in Publication Data

Cutter Costa, Cristiane Loesch de Souza.
/ Cristiane Loesch de Souza Costa. – São José dos Campos: INPE, 2009.
84p. ; (INPE-XXXX-XXX/XX - versão X)

() – Instituto Nacional de Pesquisas Espaciais, São José dos Campos, 2009.

1. Coronal mass ejection (CME). 2. Magnetohydrodynamics (MHD) simulation. 3. Solar corona. 4. Magnetic field configuration. 5. Interplanetary shocks. I. Signatures of Two Distinct Driving Mechanisms in the Evolution of Coronal Mass Ejections in the Lower Corona. Ejeção de massa coronal (CME), Simulação magnetohidrodinâmica (MHD), Coroa solar, Configuração do campo magnético, Choques interplanetários.

CDU

ATENÇÃO! A FOLHA DE APROVAÇÃO SERÁ INCLUIDA POSTERIORMENTE.

Dr. Sérgio Dasso _____

Dr. Vera Jantenco-Pereira _____

Dr. José Augusto Bittencourt _____

Dr. Abraham Chian Long Chian _____

Dr. Alisson Dal Lago _____

Dr. Merav Opher _____

Dr. Maria Virgínia Alves _____

"The important thing is never to stop questioning".

Albert Einstein

To my beloved husband ...

ACKNOWLEDGEMENTS

I would like to thank those who directly and indirectly were there with me during this journey to achieve my dream: my parents, my sister, my friends, and my family for their support and encouragement, for understanding my absence at important moments and for being there with me even that only in thought. I could not do this without you.

My professors for sharing with me their knowledge. My colleagues from INPE for the good times we spent together supporting each other through the journey.

My co-workers and friends: Flávia, Fernando and Júnior for their fellowship, for helping me and for exchanging ideas in moments of doubt. And, of course, for the moments of joy and crazy discussions just to have some fun when everything around sounds crazy.

A special thanks to those who were there with me during one of the most amazing experiences I have ever had. And, made my time in the USA unforgettable: Katie, Katie, Chet, Chris, Dana and Aline (my american "family"), Rebekah, Yong, Maurizio, Ami, Bruna, Andrea, Paula, Daniel, Marcos e Rodrigo. Without you things would be much harder. For Aline, Rebekah and Yong I also thanks for the patience, the discussions and their contribution to this work.

To César, my husband and best friend, who was always there for me, even when we were not side by side. Who believed in me and helped me in every way he could. I love you.

To CAPES (Fundação de Aperfeiçoamento de Pessoal de Nível Superior), for the financial support during my PhD research and to INPE (Instituto Nacional de Pesquisas Espaciais), for the enriching opportunity and for providing means for me to perform my job.

To JPL (Jet Propulsion Laboratory) and NASA-AMES for providing the computational resources needed to develop my simulations.

To Dr. Chip Manchester who helped and advised me during the simulation and the results discussion. Thank you for being there for me and for sharing your wide knowledge.

To Dr. Tamas Gombosi for letting me use the SWMF code.

To Dr. Alex Wuensche, my former advisor, who decided almost 10 years ago that I was worth. And, introduced me to the stars. I will be always thankful.

And last, but not least, to my advisors Dr. Maria Virgínia Alves and Dr. Merav Opher, for their incentive, support, for sharing their knowledge, for arguing, and for all the time they spent with me trying to make this work the best it can be. For their friendship, and most important for believing in me and for helping me in the accomplishment of this project (my dream).

ABSTRACT

Coronal mass ejections (CMEs) are the major driver for space weather disturbances. Their physical mechanisms and their influence on the geospace environment are the subject of active research and debate. Our goal is to understand how the initial magnetic configuration of a CME affects its evolution through the lower corona, until $6\,R_{\odot}$. We compare our results from three-dimensional simulations of CMEs, in the lower corona, driven by two different flux rope mechanisms presented in the literature: Gibson & Low (1998) (as GL98 hereafter) and Titov & Démoulin (1999) (as TD99 hereafter). The simulations are performed using the Space Weather Modeling Framework during the solar minimum (CR1922). We investigate the variation of the CME plasma density, velocity, magnetic field along the line going from the center of the Sun to the center of the flux rope. We also compare the behavior of the driven shock and the CME structure reproduced by the models. We find that both models present a quasi-parallel shock with a higher compression in GL98 case. A post-shock compression is also present showing a tendency to increase with the distance from the Sun. The GL98 model presents a faster shock speed and a higher Mach number, indicating a higher compression in the lower corona, and implying that for this model the particle acceleration can be more efficient than for TD99. The sheath in the GL98 model presents a slightly larger expansion. We also analyze the influence of the total pressure, drag and gravity forces during the CME evolution, within the same region. Results show that the magnetic pressure plays an important role for both models. The results obtained in this thesis indicate that understanding the role of magnetic fields in the initiation of CMEs is a crucial issue to study the CME evolution close to the Sun. This thesis intends to serve as a prototype for future comparisons of CME evolution, in the lower corona.

ASSINATURAS DE DOIS MECANISMOS DISTINTOS NA EVOLUÇÃO DE EJEÇÕES DE MASSA CORONAL NA BAIXA COROA

RESUMO

As ejeções de massa coronal (*coronal mass ejections* - CMEs) são as maiores causadoras das perturbações do clima espacial. Seus mecanismos físicos e sua influência no ambiente geoespacial são foco importante em debates e pesquisas. Nosso objetivo é compreender como a configuração magnética inicial da CME afeta sua evolução na baixa coroa, até $6\,R_\odot$. Neste trabalho apresentamos uma comparação entre a simulação tri-dimensional de duas CMEs, inicializadas por dois mecanismos apresentados na literatura: Gibson & Low (1998) e Titov & Démoulin (1999) (identificados a partir daqui como GL98 e TD99, respectivamente). Tais simulações foram realizadas na baixa coroa para um período do mínimo solar (CR1922) utilizando-se o código *Space Weather Modeling Framework*. A variação da densidade de plasma, velocidade e campo magnético das CMEs foram aqui investigadas ao longo de uma linha traçada do centro do Sol ao centro do *flux rope*. Também comparamos o comportamento do choque gerado pela CME e a estrutura da CME reproduzida pelos modelos. Nossos resultados mostram que ambos os modelos produzem choques quasi-paralelos, dentre eles GL98 apresenta maior compressão. Observamos, também, a presença de uma compressão pós-choque, que tende a aumentar à medida que a CME se distancia do Sol. O modelo GL98 apresenta um choque mais rápido e um maior número de Mach, indicando uma maior compressão na baixa coroa, o que implica que GL98 deveria acelerar partículas mais eficientemente do que TD99. A largura do sheath do CME é levemente maior, também, para o modelo GL98. Além disso, analisamos a influência da pressão total, da força de arrasto e da gravidade na evolução da CME, nesta região. Observando que o papel da pressão magnética no processo é importante para a evolução de ambos os modelos. Nossos resultados indicam que o papel do campo magnético na iniciação da CME é crucial para entender sua evolução próximo ao Sol. Esta tese pretende servir como um protótipo para futuras comparações da evolução da CME na baixa coroa.

CONTENTS

Pág.

LIST OF FIGURES

Pág.

1 INTRODUCTION

The Sun-Earth system have always been affected by changes in the Sun behavior. Such changes can not only affect the functioning of technical systems in space and on Earth, but may also endanger human health and life. It became important to understand the solar activity effects in the Earth's vicinity and its role on space weather, i.e. the conditions on the Sun itself and in the solar wind, magnetosphere, ionosphere, and thermosphere.

The Sun is a main sequence star which energy is produced by nuclear fusion reactions that occur deep inside its core. It consists of $\sim 71\%$ of hydrogen and $\sim 27\%$ of helium, the $\sim 2\%$ remaining matter consists of seven other elements, like oxygen, carbon, etc.

The Sun's interior can be divided in three layers: the *core*, the *radiative zone* and the *convection zone*. After being produced in the core by nuclear fusion, the Sun's energy is transferred to its outer layers. The region surrounding the core of the Sun is known as the radiation zone, where energy is transferred by radiation. The radiative zone is a very opaque region meaning the radiation undergoes many deflections; and its temperature is cooler than in the core ($\sim 1.5 \times 10^7$ K). Right above we have the convection zone, where the temperature decreases with radius. In the convection zone the energy is transferred via thermal convection leading the material to the Sun's surface. It is a less dense and less hot layer (KIVELSON; RUSSEL, 1995).

The Sun's visible surface is called *photosphere*. It is a thin layer of plasma (~ 500 km) responsible for most part of the solar radiation emission. Its temperature is about 6000 K. In the photosphere, cooler regions that appear to be darker than the neighborhood are called *sunspots*. Right above the photosphere we have the Sun's *chromosphere*, a layer less denser than the photosphere and more transparent to the solar electromagnetic radiation. Its main characteristic is a rise in temperature, reaching values between 10000 K to 20000 K. The name chromosphere comes from its reddish color, that is visible during a total eclipse. In this region solar flares and loops of hot gases can be observed.

The outer part of Sun's atmosphere is called *corona*. Right above the chromosphere, the corona is a highly rarified region that extends for millions of kilometers. The corona presents itself as a large halo of gas emission with high temperatures

($\sim 10^6$ K) and in continuous expansion. The outer edges of the corona are constantly being transported away generating the *solar wind*. Usually the corona can not be seen due to the brightness of the photosphere, except during a total solar eclipse. Figure 1.1 shows the overall structure of the Sun, including its interior and its atmosphere with the three layers: photosphere, chromosphere and corona.

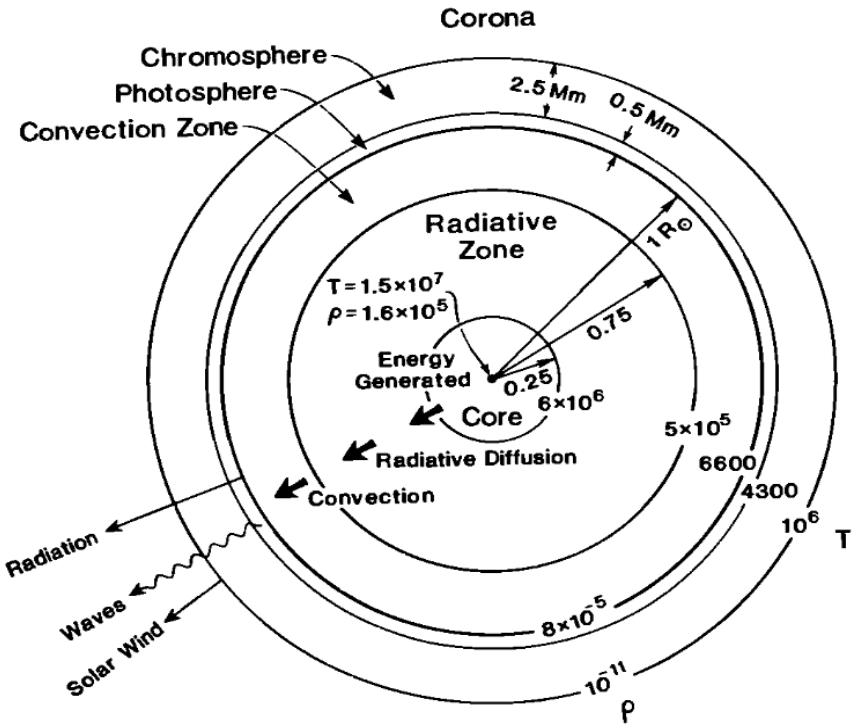

FIGURE 1.1 - Sun's interior and atmosphere structure.

SOURCE: Kivelson & Russel (1995)

The solar wind (SW) is a stream of charged particles (plasma) flowing supersonically and radially outward from the solar corona, towards the interplanetary medium. The average velocity, of about 400 km/s, results from a large pressure difference between the corona and the interplanetary medium, which leads the plasma outwards the Sun, despite the solar gravity influence (KIVELSON; RUSSEL, 1995; LYON, 2000).

The SW average temperature is $\sim 10^5$ K and it is mostly consisted of ionized hydrogen. It has a highly variable behavior and its parameters (numerical density, magnetic field, etc) change within the distance from the Sun (PARKS, 1991). Near Earth the SW average velocity is ~ 450 km/s, although closer to the Sun it depends on the origin region. The portion of the SW that comes from the polar coronal holes and reaches ~ 800 km/s is called *fast solar wind*; and the one with velocity range around 300 km/s that originates from areas closer to the equatorial regions of the Sun is called *slow solar wind* (McCOMAS et al., 1998). The slow solar wind is slower, denser and more variable then the fast one.

Because the SW plasma is highly conductive it drags the Sun's magnetic field lines with it, forming the *interplanetary magnetic field* (IMF). Due to the Sun rotation and because of the solar magnetic field lines are frozen into the radial out flowing solar wind, the IMF adopts an spiral configuration. This spiral shape, illustrated on Figure 1.2, was named *Parker spiral*.

The SW and the Sun's magnetic field characteristics also depend on the solar activity cycle, that spans approximately 11 years, from solar minimum (maximum) to solar minimum (maximum). The solar cycle is characterized by the number of sunspots in the Sun. During the solar minimum a reduced number of sunspots can be observed in high solar latitudes. While the cycle evolves the sunspots become larger, more numerous and closer to the solar equator, heading to the maximum solar activity. After that, the number of sunspots decreases gradually and the cycle decays to its minimum again. So, during the 11 year cycle the number of sunspots are a good indication of the solar activity. Every 2 solar cycles (~ 22 years) we have one solar magnetic cycle, when the solar magnetic field reverses polarity.

The solar magnetic field configuration changes throughout the solar cycle. Its configuration, at the beginning, resembles a dipole with helmet streamers around the Sun's equator and coronal holes near the poles. The axis of dipole is aligned with the Sun's rotation axis. In this configuration, the closed magnetic field lines are found near the solar equator, the open lines are in higher-latitudes and a current sheet is formed. Once the cycle evolves towards the maximum this dipole structure starts to change, the Sun is then found in a disorganized state, streamers and coronal holes are scattered all over different latitudes. During the last phase of the cycle the dipole field starts, then, to be restored.

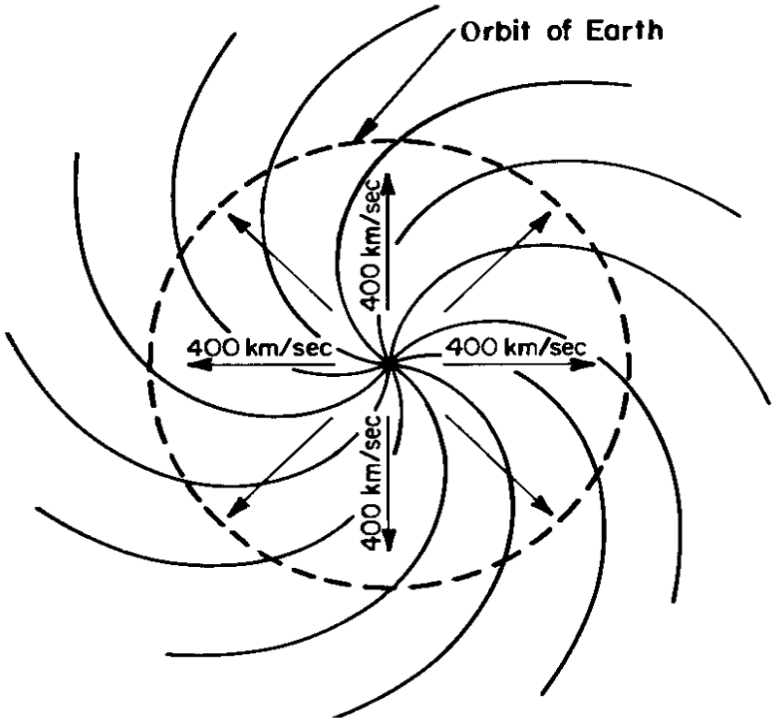

FIGURE 1.2 - Interplanetary magnetic field spiral (lines frozen into a radial solar wind expansion at $400\,\mathrm{km/s}$).

SOURCE: Kivelson & Russel (1995)

Similar changes happen to the SW structure while the solar cycle evolves. During the declining phase and the minimum phase of the solar cycle, the SW presents the bimodal structure, mentioned earlier. A fast wind coming from higher latitudes originated in polar coronal holes and a slow wind associated to the streamers in the coronal equator. Once the cycle starts to ascend and during its maximum phase, the average solar winds slows down, the fast wind flows are narrowed and weaker. But, at the same time, explosive eruptions of coronal plasma reach their peak of occurrence at the solar maximum. And, the ambient solar wind is increasingly disturbed.

What most concerns space weather researchers about solar activity is how it can affect the Earth's neighborhood. Specially because some of most dramatic phenomena on the Sun are related to the release of solar material into the interplanetary space. Such release can be associated mostly to three solar phenomena: prominences,

solar flares and coronal mass ejections. Studying these phenomena is a good start to understand how space weather develops and how to prevent some of its effects near Earth.

1.1 CORONAL MASS EJECTIONS

Considered one of the most energetic contributors to space weather, coronal mass ejections (CMEs) play an important role in the Sun-Earth connection. CME-driven interplanetary disturbances in the solar wind often affect the environment around Earth and are the primary cause of major geomagnetic storms (GOSLING, 1993; TSURUTANI; GONZALEZ, 1998).

CMEs are extreme solar activity manifest observed as bright arcs by coronagraphs (see Figure 1.3) (HUNDHAUSEN et al., 1984; SCHWENN, 1996). They are large-scale expulsions of plasma and magnetic field from the solar corona to the interplanetary space. During a CME event, $\sim 10^{16}$ g of coronal material with energies of $\sim 10^{32}$ ergs are ejected from the Sun (HUNDHAUSEN, 1997; VOURLIDAS et al., 2002).

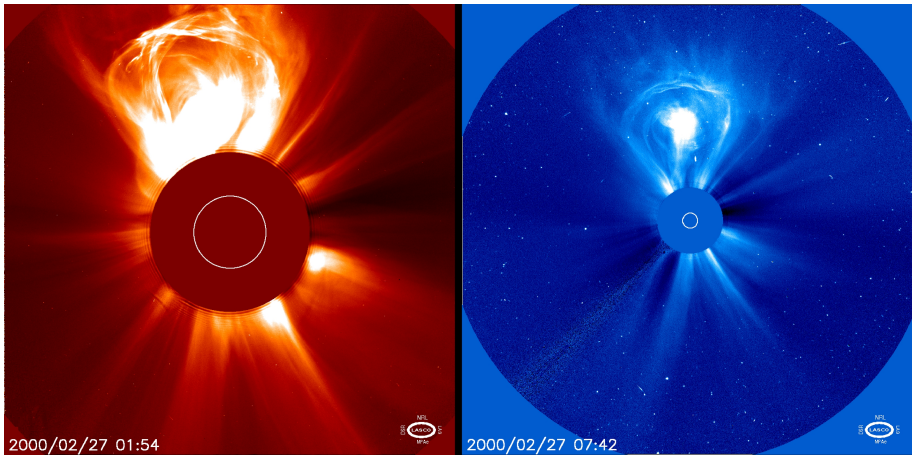

FIGURE 1.3 - A CME observed by LASCO C2 and C3 on February 27, 2000.

SOURCE: SOHO (ESA and NASA) (2006)

CMEs frequency of occurrence varies with the 11-year solar activity cycle. Near the solar activity minimum they occur on a rate of ~ 0.2 events per day, while near solar activity maximum the occurrence rate is of ~ 3.5 events per day (WEBB; HOWARD,

1994).

While propagating away from the Sun, CMEs present a speed range from a few tens up to $\sim$ 2500 km/s. Fast CMEs can be decelerated and slower ones can be accelerated by the ambient solar wind flow. Those CMEs exceeding the Alfvén speed can eventually drive fast shocks ahead of them. CME-driven fast shocks are able to accelerate charged particles up to very high energies (GeV/neutron) (WANG; WANG, 2006).

In their propagation path, CMEs leave signatures in the solar wind, such as low plasma beta, and smooth field rotations (BURLAGA, 1991). Those signatures are then related to the interplanetary counterparts of CMEs that are frequently called *Interplanetary Coronal Mass Ejections* (ICMEs).

At least 1/3 of all ICMEs are known as *magnetic clouds* (MCs) (BURLAGA et al., 2002). They can be identified by their lower temperature and higher magnetic field strength than the average and the smooth rotation of the magnetic field direction (BURLAGA, 1991). Besides MCs and shocks, solar eruptions can mostly be associated to multiple magnetic clouds and ejecta. The later are defined as fast flows moving towards Earth that are neither co-rotating flows nor magnetic clouds. It is believed that they result from the merger of the successive CMEs and that the individual characteristics of the CMEs cannot be identified. This suggests a nonlinear and irreversible merging process (BURLAGA et al., 2002). ICMEs are an important part of the chain of events for the space weather; originating on the Sun and evolving into the solar wind. When near-Earth space, they can cause geomagnetic storms.

To understand CMEs and their influence on the geospace environment, it is important to comprehend how they initiate, erupt, develop and propagate through the ambient SW. Lately, effort has been devoted to developing mathematical models, using numerical or analytical methods (e.g., Gibson & Low (1998); Antiochos et al. (1999); Wu et al. (2001); Odstrcil et al. (2002); Roussev et al. (2003a); Roussev et al. (2004); Manchester et al. (2004a); Manchester et al. (2004b)), to describe CMEs initiation and evolution.

In the first works, CME simulations did not investigate its origin, they only assumed the existence of a disturbance pulse (in pressure and magnetic field) near the Sun and observed how that disturbance would change the ambient solar wind parameters

until it reaches 1 AU[1]. Recently, CMEs propagation have been numerically simulated all the way from the solar corona to 1 AU (e.g, Lugaz et al. (2005a); Lugaz et al. (2005b); Manchester et al. (2004a); Manchester et al. (2004b)).

Considering that CMEs initiation and propagation can interfere in the physical and dynamical conditions of the Sun-Earth system, simulating them has become an important tool to space weather. Unfortunately, the physical conditions of CMEs initiation and eruption are not yet well understood. Many scenarios have been proposed for their release (e.g., Forbes & Priest (1995); Linker & Mikić (1995); Antiochos et al. (1999); Titov & Démoulin (1999); Wu et al. (1999); Manchester (2003); Roussev et al. (2003a); Roussev et al. (2004)).

Nowadays, it is well accepted that CMEs derive their energy from the coronal magnetic field and that one of the CMEs onset topologies comes from the emergence of a magnetic flux rope. In flux rope models, the eruption process can generally occur once the flux rope becomes unstable or loses its equilibrium. Here we investigate two of those mechanisms: the first one is presented in Gibson & Low (1998) (GL98 from hereafter) and the other one in Titov & Démoulin (1999) (TD99 from hereafter). Both, GL98 and TD99, are analytical flux rope models that reproduce the CME - three part structure - bright front, dark void and bright core, present in observations (HUNDHAUSEN, 1987). Both models, GL98 and TD99, have been previously used on CME and CME-driven shock simulations performed by the Space Weather Modeling Framework (SWMF) or by the Block Adaptive Tree Solar wind Roe Upwind Scheme (BATS-R-US) code (LUGAZ et al., 2005a; LUGAZ et al., 2005b; LUGAZ et al., 2007; MANCHESTER et al., 2004a; MANCHESTER et al., 2004b; MANCHESTER et al., 2005; ROUSSEV et al., 2003a; ROUSSEV et al., 2004; LIU et al., 2008).

We use GL98 and TD99 in a modified version (see Chapter 2) to trigger a CME simulation, using the SWMF. Our goal is to compare the signatures of the two different driven mechanisms on CME propagation in the lower corona (from $\sim 2\,R_\odot$ to $\sim 6\,R_\odot$, where $R_\odot$ is the solar radius). We analyze the mechanism signatures only at the nose of the CME. This can serve as a prototype to explore signatures of mechanisms of CMEs in their propagation.

The organization of this thesis is as follows. On Chapter 2 we review concepts on

[1]AU stands for astronomical unit. An astronomical unity is approximately the mean distance between the Earth and the Sun, $1\,AU \sim 150 \times 10^6$ km.

numerical simulation and the SWMF. On Chapter 3 we describe the numerical simulation set-up including the background solar wind and the driving CME mechanisms. On Chapter 4 we present the comparison between the two models, considering the evolution of the shock and the CME kinematics. A discussion of the results and the conclusions are presented on Chapter 5.

2 SIMULATION OF CORONAL MASS EJECTIONS

CMEs are the major driver for space weather disturbances. Their physical mechanisms and their influence on the geospace environment are the subject of active research and debate. The development of new tools to enhance our understanding of them and their environment became very important for space weather's forecasting.

Global magnetohydrodynamic (MHD) models represent one of these powerful tools. They have been successfully used on simulating the solar corona (USMANOV, 1995; LINKER; MIKIĆ, 1995; LINKER et al., 1999; COHEN et al., 2007), the interplanetary medium (PIZZO, 1991; ODSTRCIL; PIZZO, 1999a; ODSTRCIL; PIZZO, 1999b) and the Earth's magnetosphere and ionosphere system (OGINO; WALKER, 1984; LYON et al., 1986; RIDLEY A. J.AND RICHMOND et al., 2003; KUZNETSOVA et al., ; ZHANG et al., 2007). They have been also used on interpreting and connecting solar with in situ observations (LINKER et al., 1999).

Simulating the evolution and propagation of a CME from the Sun to the Earth has been the focus of numerous works. CMEs complex structure and dynamics lead to a diverse number of models. Numerical studies had provided a physical insight about their interaction with the ambient solar wind and their propagation away from the Sun (ODSTRCIL; PIZZO, 1999b). Recently, their propagation from the inner corona to 1 AU has been numerically modeled by two-dimensional (2D) (e.g, Odstrcil et al. (2002); Wu et al. (1999)) and three-dimensional (3D) models (GROTH et al., 2000; MANCHESTER et al., 2004b; ODSTRCIL et al., 2002). For example, Wang et al. (2002) simulated a CME propagation with a 2D MHD model. A 3D MHD model was used to simulate the CME's interaction with the bimodal solar wind (MANCHESTER et al., 2004b) and the interaction of two CMEs and their propagation from the Sun to the Earth (LUGAZ et al., 2005b).

Although a significant observational and theoretical progress has been made on understanding such events, many questions concerning CMEs remain unanswered. For example, the physical mechanisms that trigger CMEs are still unknown. Many scenarios have been proposed for their release. These various models differ by the details on which the eruption of a CME is achieved. However, there is a consensus that CMEs derive their energy from the coronal magnetic field (FORBES et al., 2006).

Numerical models usually relate the eruption process of a CME to two different

topologies: sheared magnetic arcades and the emergence of a magnetic flux rope. Both CME scenarios lead to a flux rope structure after the eruption, that can generally occur once the flux rope or arcade becomes unstable or loses its equilibrium. In the first topology, sheared magnetic arcades are the initial structures and a flux rope is formed in the course of the eruption (FORBES; PRIEST, 1995; LINKER; MIKIĆ, 1995; ANTIOCHOS et al., 1999; MANCHESTER, 2003; ROUSSEV et al., 2004). The second one assumes that the flux rope exists prior to the eruption (GIBSON; LOW, 1998; TITOV; DÉMOULIN, 1999; WU et al., 1999; ROUSSEV et al., 2003a). Chen (1996) model, for example, assumes an initial flux rope in MHD equilibrium, and the eruption occurs due to the "injection" of poloidal magnetic flux into the flux rope. Another model is the breakout model, in which the flux rope is twisted and later breaks out to initiate a CME due to a photospheric shear flow (ANTIOCHOS et al., 1999). Wu et al. (2000) illustrate the use of three different CMEs initiation processes using three observed CME events and numerical MHD simulation models. They concluded that 2 CMEs are related to streamer and flux rope magnetic topology, while one is completely different. It has no obvious relation with flux ropes, and occurs in the boundary region of a coronal hole and a streamer. In this case, the high-speed solar wind played an important role in producing the morphology of the CME.

The Space Weather Modeling Framework is a global 3D MHD model, developed by the University of Michigan, that integrates in a high-performance framework, numerical models from the solar corona to the planet's upper atmosphere for space weather simulations (TÓTH et al., 2005). It has been used, for example, to simulate CMEs and CMEs-driven shocks (LUGAZ et al., 2005a; LUGAZ et al., 2005b; LUGAZ et al., 2007; MANCHESTER et al., 2004a; MANCHESTER et al., 2004b; MANCHESTER et al., 2005; ROUSSEV et al., 2003a; ROUSSEV et al., 2004; LIU et al., 2008). These CME simulations were performed by two different flux rope models: Gibson & Low (1998) and Titov & Démoulin (1999). More recently, Holst et al. (2007) simulated a CME initiation and evolution using a breakout model. In the next two sections we will briefly describe the SWMF and the two driving (GL98 and TD99) CME models.

2.1 SPACE WEATHER MODELING FRAMEWORK (SWMF)

Developed by the Center for Space Environment Modeling (CSEM) at the University of Michigan and its collaborators, the SWMF enables simulations of different domains of the Sun-Earth system. This global 3D MHD adaptive mesh refinement (AMR) code was designed to incorporate different computational physics modules

in an efficient manner, so its individual domains may interact or overlap with each other. With SWMF, space weather simulations can be performed on massively parallel supercomputers, with high spatial and temporal resolution.

On SWMF the solar corona, the solar wind and the magnetospheric dynamics are described by ideal MHD equations. The set of MHD equations describes the transport of mass, momentum, energy and the evolution of the magnetic field. The magnetic field evolution is given by the Faraday's law with an infinite electrical conductivity.

The MHD equations written in conservative form are (POWELL et al., 1999; GROTH et al., 2000; MANCHESTER et al., 2004a; LUGAZ et al., 2005a):

$$\frac{\partial \rho}{\partial t} + \nabla \cdot (\rho \mathbf{u}) = 0, \tag{2.1}$$

$$\frac{\partial (\rho \mathbf{u})}{\partial t} + \nabla \cdot \left[\rho \mathbf{u}\mathbf{u} + \left(p + \frac{B^2}{8\pi} \right) I - \frac{\mathbf{B}\mathbf{B}}{4\pi} \right] = \rho \mathbf{g}, \tag{2.2}$$

$$\frac{\partial \mathbf{B}}{\partial t} + \nabla \cdot (\mathbf{u}\mathbf{B} - \mathbf{B}\mathbf{u}) = 0, \text{ and} \tag{2.3}$$

$$\frac{\partial \varepsilon}{\partial t} + \nabla \cdot \left[\mathbf{u} \left(\varepsilon + p + \frac{B^2}{8\pi} \right) - \frac{(\mathbf{u} \cdot \mathbf{B})\mathbf{B}}{4\pi} \right] = \rho \mathbf{g} \cdot \mathbf{u}, \tag{2.4}$$

where the total energy density ε is given by

$$\varepsilon = \frac{\rho u^2}{2} + \frac{p}{\gamma - 1} + \frac{B^2}{8\pi}, \tag{2.5}$$

and ρ is the plasma mass density, $\mathbf{u}$ the plasma velocity, $\mathbf{B}$ the magnetic field, and p is the plasma pressure (sum of electron and ion pressures). Finally, the gravitational acceleration $\mathbf{g}$ is given by:

$$\mathbf{g} = -g \left(\frac{\mathbf{r}}{r} \right) \left(\frac{R_\odot}{r} \right)^2, \tag{2.6}$$

where $R_\odot$ is the radius of the Sun and g is the solar surface gravitational acceleration. In Equation 2.5 gravity is omitted from the total since it is treated as a momentum source term. The polytropic index (γ) will be discussed in the next Chapter, since in our work we use a nonuniform spatial distribution of γ. These equations are then

put in a dimensionless form, using density and ion-acustic wave speed values from a suitable part of the domain (in our case the low corona) in addition to a reference length scale (in this case the solar radius), before they are solved.

Currently, nine different physical models integrate SWMF. These models range between the solar surface to the planet's upper atmosphere. The SWMF nine components are: Solar Corona (SC); Eruptive Event Generator (EE); Inner Heliosphere (IH); Solar Energetic Particles (SP); Global Magnetosphere (GM); Inner Magnetosphere (IM); Radiation Belt (RB); Ionosphere Electrodynamics (IE); and, Upper Atmosphere (UA). Figure 2.1 illustrates the components of the framework. Their full description is presented in Tóth et al. (2005).

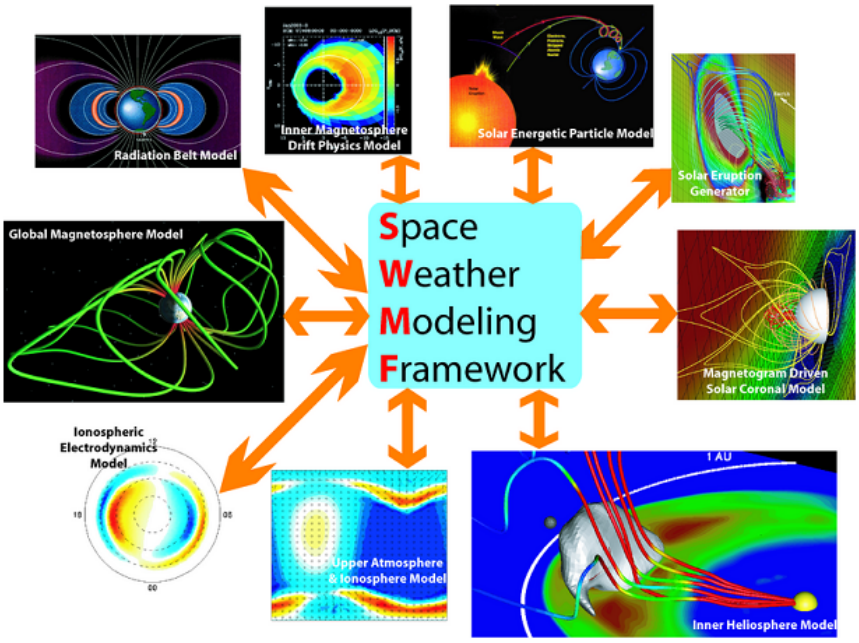

FIGURE 2.1 - SWMF's nine physics domains.

SOURCE: Tóth et al. (2005)

Dividing the work to different components has the advantage of allowing each one to have it's own equations, coordinate system, grid refinement and numerical schemes, that can be optimize for each specific physics domain. Since each component is

responsible by solving its own equations and on receiving and providing information from/to the other domains, a more accurate representation of the domains can be achieved. On a CME simulation from the Sun to the Earth, for example, three of these components have to be combined SC, EE and IH. The steps to be followed are:

a) An steady state solar wind solution, from the corona ($\sim 1\,R_\odot$) to $\sim 24\,R_\odot$, is generated by the SC component;

b) The IH component combines itself to the SC component to obtain an steady state solar wind solution from $\sim 20\,R_\odot$ to ~ 1 AU;

c) The EE component, embedded in the SC component, initiates a CME by adding a flux rope to the SC solution;

d) The SC and IH components allow the CME's propagation to get to the Earth's neighborhood.

The core of the SWMF's simulations (components SC, IH and GM) is performed based on the Block Adaptive Tree Solar-wind Roe Upwind Scheme (BATS-R-US) (POWELL et al., 1999). Designed for space physics applications, the BATS-R-US is a very efficient parallel MHD code, based on a block adaptive cartesian grid. Its parallel execution is realized by Message Passing Interface (MPI). And, its grid refinement and MHD equations solution is done by AMR techniques, that adapt the computational grid automatically. BATS-R-US has been successfully used for the global MHD simulation of space weather (GROTH et al., 2000; MANCHESTER et al., 2005). Its ideal MHD equations allow it to describe the dynamic behavior of the corona, solar wind, interplanetary medium and magnetospheric plasma (GROTH et al., 2000).

Figure 2.2 illustrates the domain extention of the SWMF components, although it is presented out off scale. Among all SWMF domains, to simulate a CME in the inner corona we will use only the SC component, presented in dark blue in the figure.

The SC component has its domain extended from $1\,R_\odot$ (low corona) to $\sim 24\,R_\odot$. Currently, its physical model drives a steady state solar wind solution from an incorporated magnetogram used as a realistic boundary condition for the Sun's magnetic field (ROUSSEV et al., 2003b; COHEN et al., 2007). It can be in an inertial or rotating

frame. The SC component can be combined with the IH and SP domains, providing the plasma variables at the inner boundary of the inner heliosphere or the plasma and magnetic field parameters for the solar energetic particles.

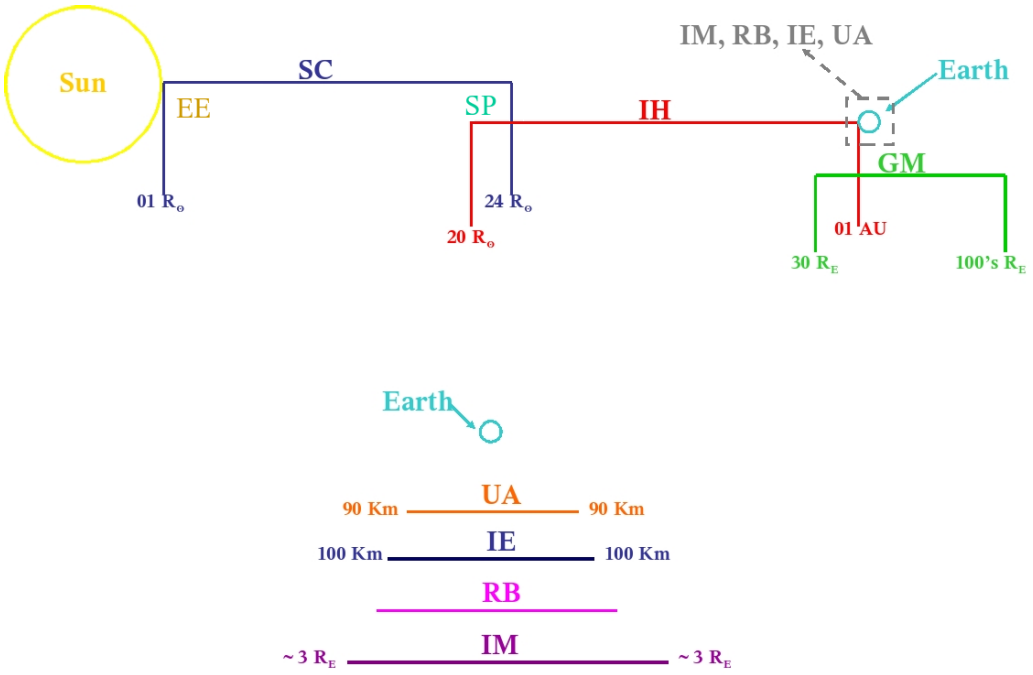

FIGURE 2.2 - Illustration, out of scales, for the domain extension of the SWMF components.

Restricted to the eruptive event (typically a CME), the EE component can be represented as a boundary condition for the SC component or as a perturbation of the SC solution. In the current SMWF version, the CME eruptive generator is presented in two versions that allows superimpose a magnetic flux rope to the SC solution. One version uses the Gibson & Low (1998) model and the other uses the Titov & Démoulin (1999) model in a modified version (ROUSSEV et al., 2003a) (they will be discussed in the next session). Both these models can be used separately or together. The code input set up is organized in certain way that allows the user to combine these models as, for example, to initiate a CME with GL98 and a few minutes later initiate another one with TD99. Recently, another CME initiation mechanisms have been developed in BATS-R-US, the shear motion (ROUSSEV et al., 2007). Manchester (2007) examined the dynamic of shearing motions between the solar atmosphere layers in order to explain how the coronal magnetic field become energized to produce

CMEs and two-ribbon flares. And, Holst et al. (2007), using the breakout model, showed that a CME ejection results from a top of the streamer if the initial topology is located underneath the helmet streamer of the solar wind.

2.2 THE TWO DRIVING MECHANISMS

CME initiation models still depend on the understanding of the physical conditions that lead to the eruption. Given that the physical mechanisms that trigger a CME are still unknown, both analytical and numerical models need a deeper understanding on how it happens in order to improve CME initiation models (FORBES et al., 2006). Flux rope models, for example, assume the existence of a twisted flux rope prior to the CME eruption. Although this assumption is still unclear, most of these models do not discuss the means of its formation.

In the current version of SWMF, two of these flux rope models can be used to trigger a CME: the Gibson & Low (1998) and the Titov & Démoulin (1999) in a modified version (ROUSSEV et al., 2003a). They have been previously used on CME and CME-driven shock simulations (LUGAZ et al., 2005a; LUGAZ et al., 2005b; LUGAZ et al., 2007; MANCHESTER et al., 2004a; MANCHESTER et al., 2004b; MANCHESTER et al., 2005; ROUSSEV et al., 2003a; ROUSSEV et al., 2004; LIU et al., 2008). These two mechanisms are analytical flux rope models that reproduce the CME three part structure: bright front, dark void and bright core, present in observations (HUNDHAUSEN, 1987).

2.2.1 The GL98 flux rope

In the GL98 model, the expansion of a magnetic flux rope in the inner corona is described by a 3D MHD time-dependent analytical solution (GIBSON; LOW, 1998). The flux rope solution is achieved by applying a mathematical stretching transformation to an axisymmetric, spherical ball of twisted magnetic flux in equilibrium with plasma pressure (LITES et al., 1995). Such transformation is performed in spherical coordinates. The mathematical form of GL98 is presented on Gibson & Low (1998) and Manchester et al. (2004a).

Initially, we have a toroidal magnetic rope contained in a sphere of radius r_0. Such sphere is located at a radial distance (r_1) from the center of the Sun, on the y axis. The flux rope is initially in equilibrium, its internal pressure is proportional to the magnetic field strength and plasma pressure (which are defined by the parameter a_1). This initial topology is then deformed once a stretching transformation

$r \rightarrow r - a$ is applied. Such transformation stretches space towards the origin. Its angular coordinates, however, are maintained fixed. The flux rope initially spherical is then distorted into a tear-drop shape. Figure 2.3 illustrates the transformation of a sphere $\partial\sigma$ to a tear-drop shaped region $\partial\Sigma$, where $a = r_0 - r_1$.

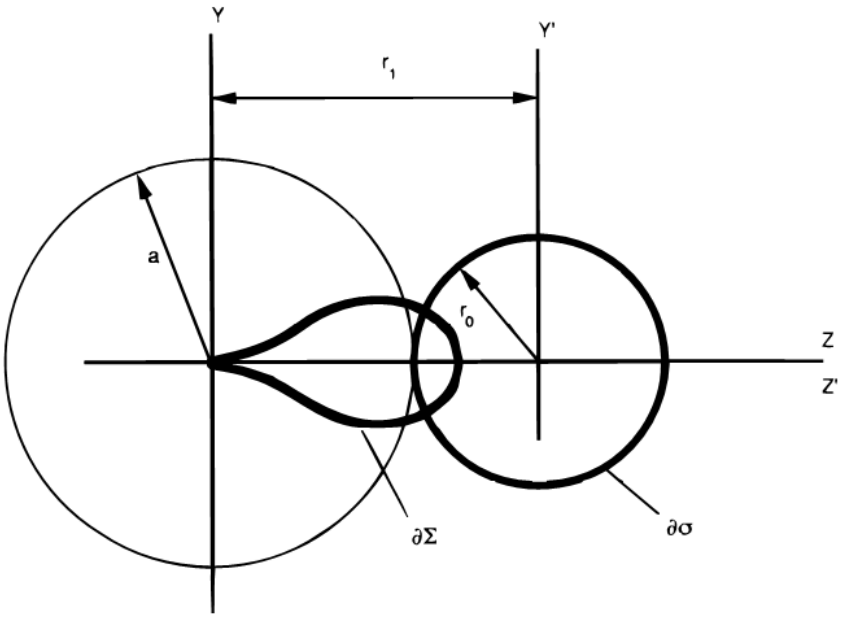

FIGURE 2.3 - Illustration of the mathematical stretching transformation of a sphere $\partial\sigma$ distorted into a tear-shaped curve. Limiting case for $a = r_0 - r_1$ where the leftmost point of the circle is mapped onto the origin.

SOURCE: Gibson & Low (1998)

This transformation generates a complex tear-drop geometric shape to the flux rope with full 3D spatial variation and introduces Lorentz forces into the system. These forces are associated with the magnetic field and require both the pressure and weight of plasma in a gravitational field to be in static equilibrium, assuring that the outward radial expansion is sustained. A cold dense plasma is necessary in regions where the magnetic field is concave away from the center of the Sun, in order to offset the upward magnetic tension. Moreover, a reduction in the plasma density is required in regions where the magnetic field is convex, so that the buoyancy offsets the downward directed Lorentz force. An attractive feature of GL98 is its density structure that presents a dense helmet streamer with an embedded cavity and a

prominence-type density enhancement. Such structures have already been observed giving rise to CMEs (HUNDHAUSEN, 1993).

In this GL98 configuration, the CME initial velocity field is purely radial and increases within the distance from the center of the Sun. Such velocity profile and a polytropic index $\gamma = 4/3$, assures the expansion of the system to evolve. While the expansion evolves, the flux rope density structure captures both the morphology and kinematic properties of a variety of CMEs.

Even with some limitations as, for example, inability of addressing the CME initiation, the GL98 model succeeds on capturing the essence of a CME, relating on a self-consistent, fully 3D MHD model, the CME density structure to its magnetic field. And, on reproducing, at least qualitatively, its observed three-part density structure and capturing its early evolution phase.

Manchester et al. (2004a) have included the GL98 flux rope onto a numerical, steady state solution of the solar corona and solar wind (performed with BATS-R-US). The flux rope was inserted in a helmet streamer and allowed to interact with a bimodal structured solar wind. Figure 2.4 illustrates a 3D representation of the solar wind and flux rope magnetic structure at $t = 0$ hours. In the figure, the yellow and orange lines represent the poloidal field of the steady state equatorial streamer belt. The red and blue lines represent the flux rope, with its highly twisted flux closer to the rope's surface and its toroidal core, respectively. The black lines in the x-z plane represent the computational mesh, superimposed to a color coded image of the velocity magnitude.

In Manchester et al. (2004a) the magnetic field and the density of the GL98 flux rope was superimposed onto a steady state solar corona. The CME results from an initial force imbalance condition. The force imbalance results from: a removal of part of the plasma in the flux rope; and, from the insufficient plasma pressure in the background corona to offset the magnetic pressure of the flux rope, that allows the magnetic forces to drive the eruption. Within this scenario, they found out that the flux rope expands rapidly, driving a strong shock ahead of it along with large amounts of plasma mimicking a CME.

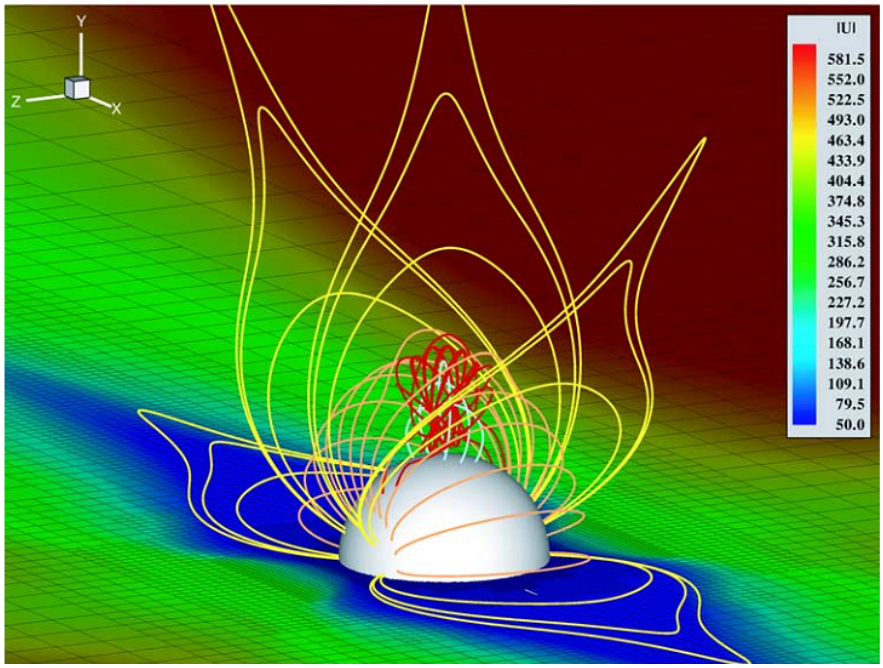

FIGURE 2.4 - Solar and flux rope magnetic structure 3D representation at $t = 0$ hours. The yellow and orange lines represent the poloidal field of the steady state equatorial streamer belt. The red and blue lines represent the flux rope, with its highly twisted flux closer to the rope's surface and its toroidal core, respectively. And, the black lines, in the x-z plane, represent the computational mesh that is superimposed to a color coded image of the velocity magnitude.

SOURCE: Manchester et al. (2004a)

2.2.2 The TD99 flux rope

The TD99 model is an analytical 3D flux rope model proposed to explain flares and CMEs. In the TD99 model, a background coronal field is assumed to be a superposition of a bipolar field plus the field of a line-current. The magnetic configuration consists in a circular flux rope embedded in a line-tying surface (TITOV; DÉMOULIN, 1999).

In this model, a force-free circular flux tube, with major radius R, is prescribed by a total toroidal current I. The flux rope is embedded into a potential background field with two different components. The first magnetic field component is created by the ring current I. The second component, a dipole field, is generated by two point magnetic charges $\pm q$ placed at a depth d beneath the so-called photosphere surface (plane z=0).

Figure 2.5 illustrates the magnetic topology of the TD99 model. In the figure, the shaded torus represents a force-free flux tube with total current I, a pair of magnetic charges $\pm q$ and an infinite line-current I_0. Beneath the photospheric plane $z = 0$, at a depth d, we have the central axis of the torus, the line-current, and the two point charges. This configuration only has physical meaning above the photospheric plane.

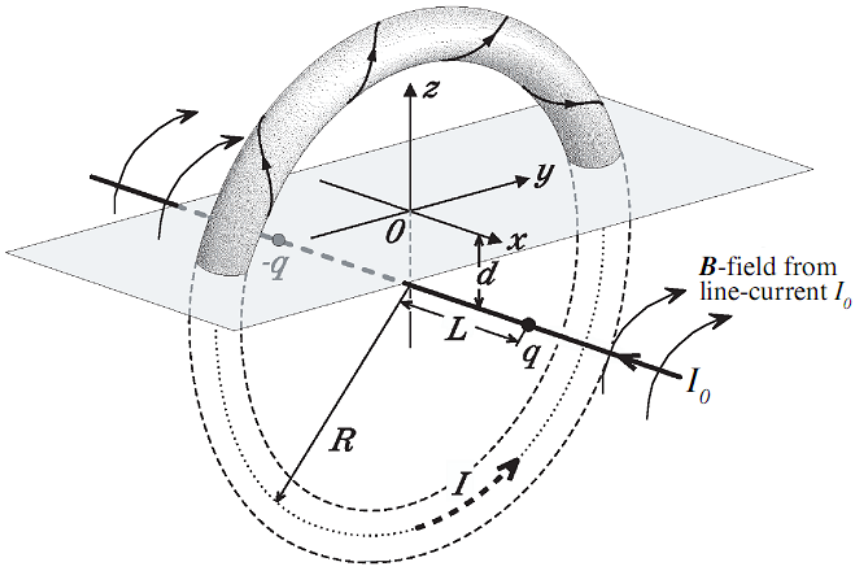

FIGURE 2.5 - Magnetic topology of the TD99 model where the shaded torus represents a force-free flux tube with total current I, a pair of magnetic charges $\pm q$ and an infinite line-current I_0. At a depth d below the photospheric plane $z = 0$ we have the central axis of the torus, the line-current, and the two point charges. The physical meaning of this topology only has physical meaning above the photospheric plane.

SOURCE: Titov & Démoulin (1999)

In addition to the field generated by the two charges, the contribution of an infinitely long-line current (I_0) is allowed. This current lies below the photosphere at a depth d. This imaginary current produces a toroidal field that reduces the number of turns of the field line within and outside the flux rope.

Analyzing the model stability, Titov & Démoulin (1999) found out that a necessary condition for the flux rope instability is that the major radius R must exceed $\sqrt{2L}$,

where L is half the distance between the background sources $\pm q$. However, they did not include the effects of the line-tying of the poloidal field circulating around the flux rope in their analysis.

In this work we use a modified version of the TD99 model. The changes in the model were motivated by the studies of Roussev et al. (2003a) who have tested the semicircular flux rope of the TD99 model in the context of CME initiation using BATS-R-US. Using the original TD99 model they found out that the flux rope would not escape in this configuration, resembling more an impulsive-type flare than a CME-like event. They realized that the arcade field associated with the sub-surface line current had to be removed, so I_0 was set to zero. With this change the flux rope would escape but the number of turns in the field lines at the surface would increase. Flux ropes with a small number of turns ($\sim 1-4$) would not manifest any loss-of-equilibrium, while the highly twisted ones (~ 200) do.

Roussev et al. (2003a) numerical study demonstrated that the instability criteria pointed out by Titov & Démoulin (1999) is not a sufficient one, and that R should have larger values, exceeding $5L$ in order to achieve an eruption resembling a CME. Figure 2.6 shows a 3D view of the flux rope configuration after the line-current removal. The solid lines represent the magnetic field lines and the color coded represents the strength of the magnetic field.

In this modified version, the flux rope is not in equilibrium with the background magnetic field. However, the forces that lead to the CME eruption have a magnetic nature. The charges and I_0 under the Sun's surface are ignored to facilitate the eruption. An extra density of $1.7 \times 10^{-17}\,\mathrm{g/cm^3}$ is introduced into the flux rope in addition to the background solar corona density to avoid effects associated to the initial transient. Moreover, inside the flux rope the kinetic pressure stays the same while the temperature inside the flux rope is decreased (LUGAZ et al., 2007).

The TD99 modified version was also used by Lugaz et al. (2007) to simulate the interaction of multiple CMEs and, most recently, by Liu et al. (2008) to simulate a CME propagation and the driven shock evolution in the lower corona.

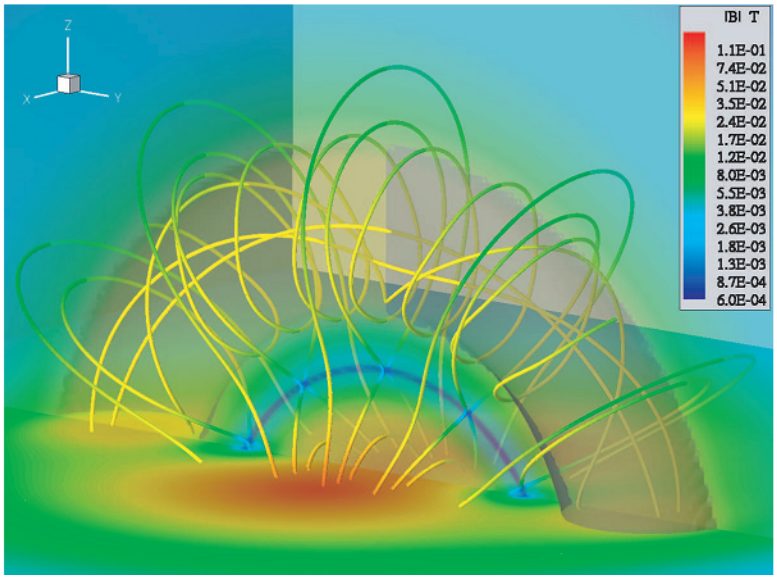

FIGURE 2.6 - 3D view of the flux rope configuration after the line-current removal. The surface shaded in gray is an isosurface of $B_z = 0$. The solid lines represent the magnetic field lines and the color coded represents the strength of the magnetic field.

SOURCE: Roussev et al. (2003a)

3 THE NUMERICAL SIMULATION

In the past few years CME modeling algorithms have improved. In the present work, we are interested on investigating the signatures and effects of two different driving mechanisms on the CME evolution in the inner corona ($\sim 2 - 6\,R_\odot$).

In our simulation an out of equilibrium flux rope is superimposed to a steady state background solar wind. In the 2007, May version of SWMF, the steady state solar wind solution is driven by an incorporated magnetogram used as a realistic boundary condition for the Sun's magnetic field (ROUSSEV et al., 2003b; COHEN et al., 2007). The CME can then be triggered by two models: GL98 or TD99. The TD99 model is presented in its modified version where the CME eruption is allowed by setting its subsurface line current to zero (ROUSSEV et al., 2003a). The GL98 model, re-inserted by us in this version of the code, drives a CME eruption by superimposing the magnetic field and the density of the flux rope onto a steady-state solar corona (MANCHESTER et al., 2004a). In this work the only SWMF component we use is the solar corona (SC).

To re-insert the GL98 subroutine into SWMF (SC), it was necessary to include the proper subroutines to allow the GL98 flux rope generation; re-define and adapt the variables related to GL98; and, define a GL98FLUXROPE command that is used to insert the input parameters (as, for example, the flux rope radius). After including the subroutines and connecting them, the results were tested to guarantee that the magnetic field and density were being calculated properly.

We run our model on a Xeon cluster with 512 processors (of 3.2 GHz each) and performance of 6.55 TFLOPS. To run our steady state we used 128 processors and 40 processors were used to run the CME evolution. Such number of processors allow us to run the steady state simulation within ~ 3 hours of real time and a 10 min CME simulation in ~ 8 hours of real time.

To start the steady state solar wind simulation we use a simulation box limited to a cubic region, that extends from $-24\,R_\odot < x < 24\,R_\odot$, $-24\,R_\odot < y < 24\,R_\odot$, $-24\,R_\odot < z < 24\,R_\odot$, centered around the Sun and with the magnetic axis aligned to the z axis. The initial grid is refined to a size $3/128\,R_\odot$ on the solar surface and each block is further divided into $4 \times 4 \times 4$ cells. For the background solar wind we have also resolved the heliospheric current sheet region, in which the blocks were

refined to a size $3/16\,\mathrm{R}_\odot$ (GROTH et al., 2000).

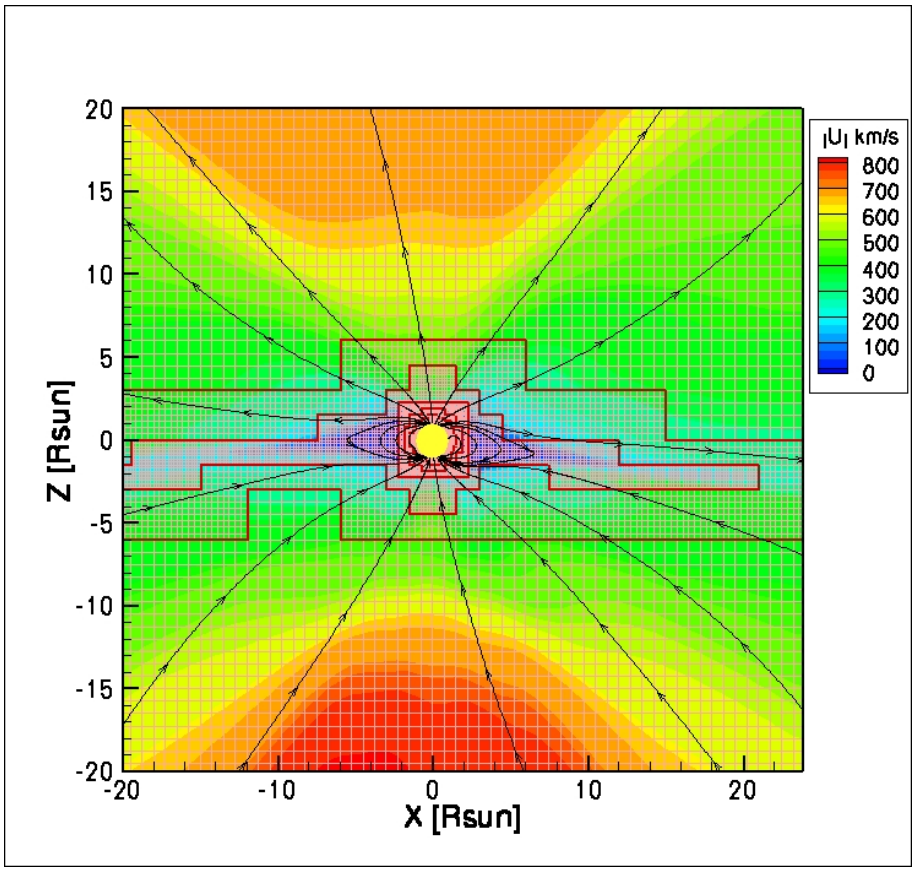

FIGURE 3.1 - Steady state solar wind grid refinement in the x-z plane: showing the grid resolution at the heliospheric current sheet. The light pink and red lines define the grid resolution regions. The solid black lines are the magnetic field lines and the color coded represents the solar wind velocity.

The blocks near the CME-driven shock center were further refined using Adaptive Mesh Refinement (AMR). We set a refinement in a region within a cone zone around the line that goes from the center of the Sun to the center of the flux rope. Near the shock the finest cell size was $3/128\,\mathrm{R}_\odot$. The time refinement of the grid is set to refine the grid before the shock arrives, increasing 2% and removing 1.5% of the grid. The pace of the refinement is initially set to every 1000 iteration steps, changing later to 5000. Figure 3.2a shows the initial grid refinement before the flux rope is inserted into the simulation ($t = 0\,\mathrm{min}$) and 3.2b shows the grid refinement after the CME has started to evolve ($t = 10\,\mathrm{min}$).

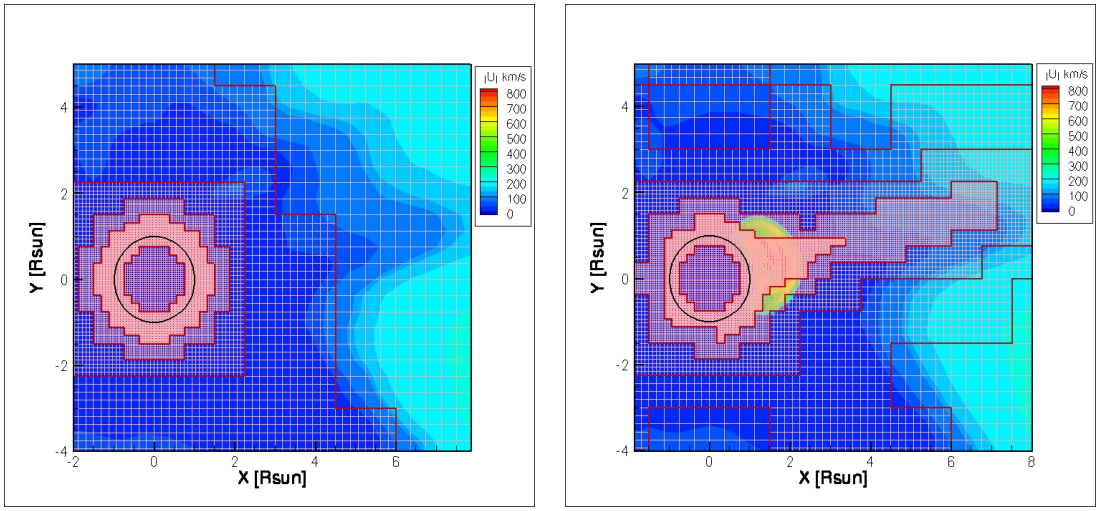

FIGURE 3.2 - Grid refinement a) at $t = 0\,\mathrm{min}$ before the flux rope is inserted into the simulation; b) near the CME-driven shock at $t = 10\,\mathrm{min}$. The black circle represents the Sun and the false color code represents the CME velocity.

3.1 The Steady State Background Solar Wind

Theoretical models still face challenges in order to provide a quantitative accurate agreement between solar wind simulations and observations at 1 AU. Two of their fundamental challenges are related to the source of the heating and acceleration of the SW.

MHD models have to consider, for example, facts as that in addition to thermal pressure some sort of momentum must be added in order to drive a more realistic background solar wind in the lower corona. Models without this additional momentum seem to have problems on matching the ratio density at both boundaries, the corona and 1 AU. Usmanov & Goldstein (2003) discuss that, in these models, once you match the density in one boundary, in the other boundary it will have a highly inaccurate value. So, to have a solar wind that match observations, one of the choices to provide momentum is the addition of Alfvén waves into the models, once they have the recognized ability of producing additional non-thermal acceleration near the Sun and at large distances. Magnetosonic waves, on the other hand, are damped close to the Sun being unable to provide the momentum within a few solar radii from the Sun. Evans et al. (2008), for example, have shown that, although MHD models are consistent on reproducing aspects of the SW at 1 AU (like density and

magnetic field), the different methods of solar wind acceleration and coronal heating are not consistent with respect to Alfvén speed in the lower corona, that is critical for the shock formation.

Our steady state SC was simulated using the model presented by Cohen et al. (2007), where the solar wind is driven by a non-uniform polytropic index distribution, also presented in Roussev et al. (2004). Such distribution is used to obtain the heating and the acceleration of the SW plasma and enables the reproduction of the bimodal solar wind (COHEN et al., 2008). The polytropic index replaces the ratio of specific heating in the ideal MHD equation of energy to include the effects of heating addition (TOTTEN et al., 1996; COHEN et al., 2008). Totten et al. (1996) suggested that the polytropic index value of 1.46 ± 0.04 is suitable for solar wind studies.

The SC model is driven by a magnetogram from SOHO Michelson Doppler Imager (MDI), during Carrington Rotation (CR) 1922. The CR1922 maps represent the photospheric magnetic field during a 27.3 days period of Sun's rotation centered on May 24, 1997, during solar minimum conditions. This CR1922 was already investigated before by Cohen et al. (2007), and Liu et al. (2008). Figures 3.3a and 3.3b show a radial field map of CR1922 from SOHO/MDI and the sintetic map for the same CR used in this work. Synoptic maps are constructed by the overlaying daily magnetograms and using a weighted mean for overlapping regions, where the weighting factor is a function of longitudinal distance (see detail in Arge & Pizzo (2000)).

The coronal radial magnetic field is determined from a potential extrapolation of the observed photospheric magnetic field provided by the magnetogram. The coronal magnetic field distribution is calculate in terms of a series of expansion of spherical harmonics by a potential field source surface (PFSS) model between $R_\odot \leq r \leq R_{SS}$, where $R_\odot$ and R_{SS} are the model inner and outer boundaries, respectively (ALTSCHULER; NEWKIRK, 1969; SCHATTEN et al., 1969; RILEY et al., 2006). In the inner boundary ($R_\odot$) the magnetic field is specified by the magnetogram. The outer boundary, R_{SS}, is a spherical equipotential surface, usually known as source surface (SS), beyond which all field lines are radial. The source surface radius is a free parameter usually set as $R_{SS} < 2.5\,\mathrm{R}_\odot$

The potential field distribution is then used in the Wang-Sheeley-Arge (WSA) model (ARGE; PIZZO, 2000; ARGE et al., 2004) to calculate an expansion factor f_s for the

magnetic flux tube, given by:

$$f_s = \frac{|B(R_{SS})|R_{SS}^2}{|B(R_\odot)|R_\odot^2} \quad . \tag{3.1}$$

Then a solar wind speed distribution, on a spherical surface at 1 AU, is provided by WSA model. This distribution is a function of f_s and the angular distance between the foot point of the magnetic field and the coronal hole boundary (ARGE et al., 2004; RILEY et al., 2006; HOEKSEMA et al., 1982).

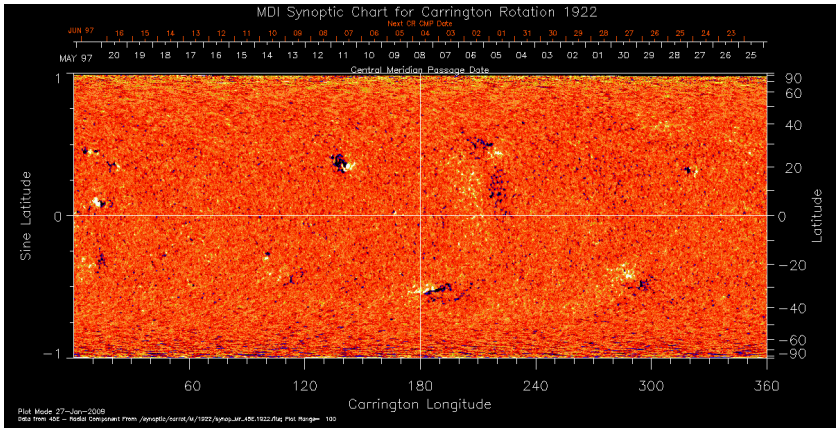

(a)

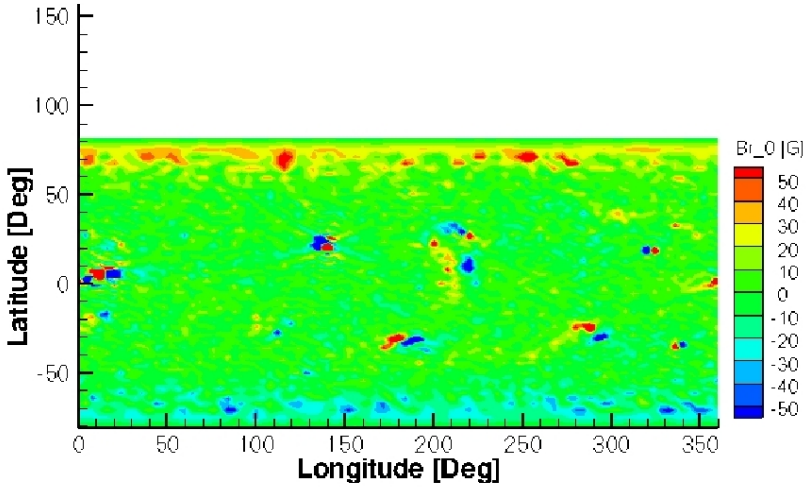

(b)

FIGURE 3.3 - Magnetograms: (a) radial field map of CR1922 from SOHO/MDI; (b) sintetic map for CR1922.

SOURCE: SOHO (ESA and NASA) (2007)

The WSA model is an empirical and physical-based representation of a quasi-steady global solar wind flow that can be used to predict the ambient SW speed and the IMF polarity at Earth (ARGE; PIZZO, 1999). In this model a PFSS model (ALTSCHULER; NEWKIRK, 1969; SCHATTEN et al., 1969; RILEY et al., 2006) obtains a potential radial field solution of the corona using ground-based line-of-sight observations of the Sun's surface magnetic field as input. The solar wind velocity is assigned at $2.5\,R_\odot$ using an empirical function relating the magnetic field expansion factor to the velocity. A Schatten current sheet (SCS) model (SCHATTEN, 1971) is used to propagate the SW from the source surface to the Earth.

Using the WSA model together with the Bernoulli integral we calculate the polytropic index (γ) distribution. At the source surface the value of γ is obtained by an interpolation of the photospheric γ value (along a magnetic field line), and it is spherically and uniformly set as 1.1. Between $2.5\,R_\odot < r < 12.5\,R_\odot$ the value of γ varies linearly between 1.1 and 1.5 (TOTTEN et al., 1996) and for $r > 12.5\,R_\odot$, γ is set as 1.5 (COHEN et al., 2007; COHEN et al., 2008). Figure 3.4 shows γ's spatial distribution.

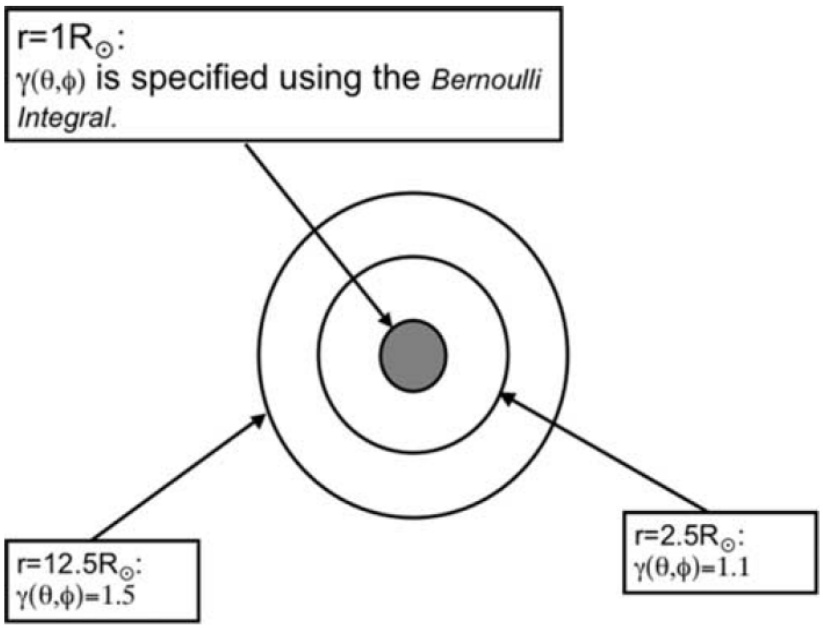

FIGURE 3.4 - Spatial distribution of the polytropic index.

SOURCE: Cohen et al. (2008)

Within the γ distribution the MHD equations are, then, solved self-consistently (GROTH et al., 2000). To calculate the solar wind solution, we set up the solar surface temperature to 2×10^6 K and the density to 5×10^{-16} g $\cdot$ cm^{-3}. After 12,000 steps, a steady state solar wind is obtained.

This steady state solution reproduces the bimodal solar wind, with the fast solar wind at high latitudes and the slow wind at low latitudes. It has the general structure of the coronal magnetic field lines, opened into the heliosphere by the fast wind. And, closed lines near the Sun's equator, with a thin current sheet formed along the surface of polarity reversal of the radial magnetic field. Besides that, the simulated temperature and density structure match observations. The resulting realistic steady state solar wind is shown in Figure 3.5, and is used as a background to drive both CMEs.

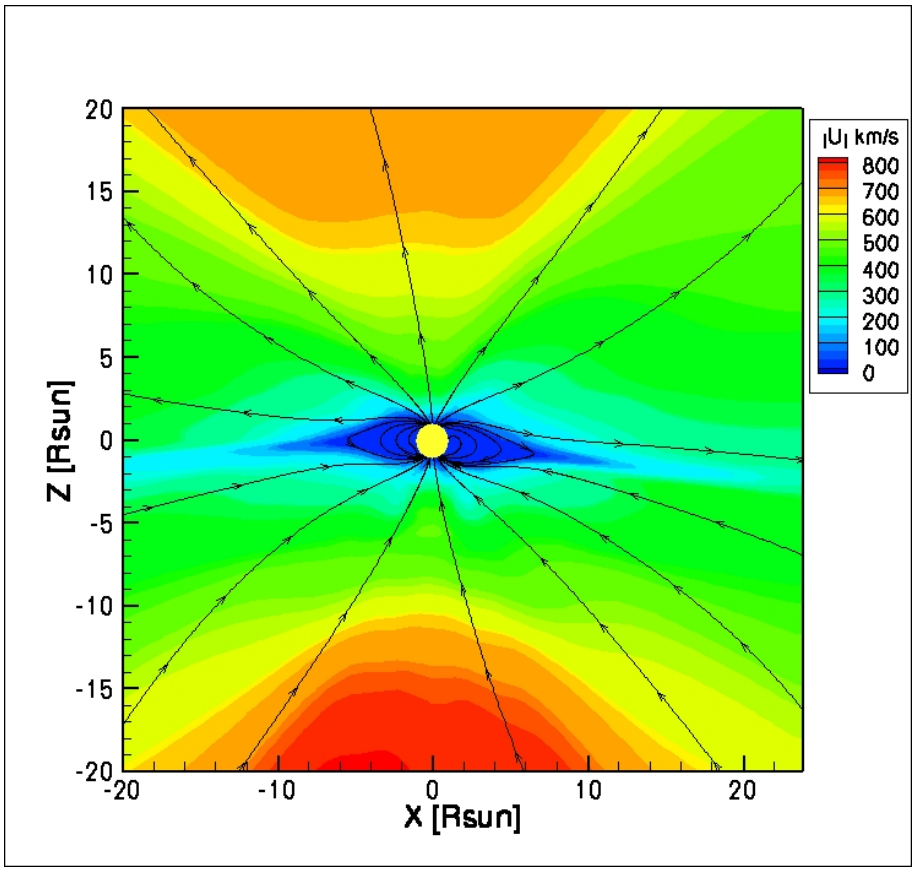

FIGURE 3.5 - Speed of steady state solar wind solution for CR1922 in the x-z plane. The solid black lines are the magnetic field lines.

3.2 CME's initiation

It is well known that the eruption of a CME can generally occurs once a flux rope or arcade becomes unstable or loses its equilibrium. However, the details of the process are yet to be determined. Here we simulate a CME with two different flux rope driving mechanisms: Gibson & Low (1998) and Titov & Démoulin (1999), to investigate the CMEs signatures during its propagation in the lower corona.

Each mechanism flux rope is superimposed within a chosen active region (AR8040) near the solar equator to the same steady state background solar wind and coronal solution (described on the previous section). This active region was chosen because it was the closest one to the solar equator in the interval defined by CR1922. Both flux ropes are centered in the same position ($x = 1.08\,\mathrm{R}_\odot$, $y = 0.27\,\mathrm{R}_\odot$, $z = 0.11\,\mathrm{R}_\odot$) and their top portion are aligned with the closed magnetic field line in the AR8040. The choice for the parallel alignment aims to minimize the transverse drift of the CME. Such flux rope configuration is the same as the one used in Liu et al. (2008). Figure 3.6 shows a three-dimensional representation of the two flux ropes models used in this work and their active region on the Sun.

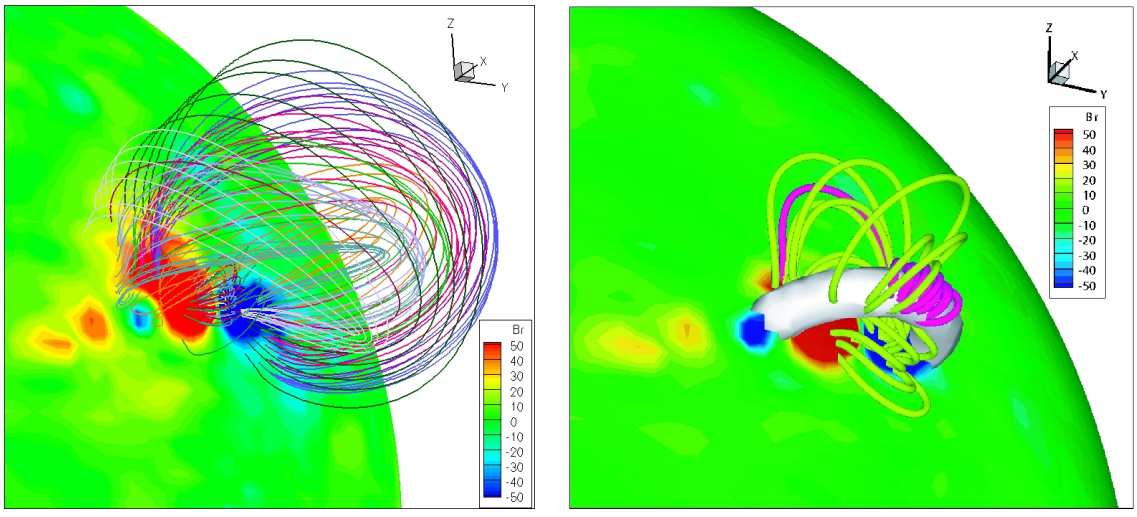

(a) (b)

FIGURE 3.6 - Three-dimensional representation of the inserted flux rope and the active region (AR8040) on the Sun. The spherical surface shows the magnetic field on the solar surface. a) shows the superimposed GL98 flux rope. The twisted magnetic field lines are drawn as colored lines; b) shows the TD99 flux rope represented by the isosurface of the current $I = 200\,\mathrm{mA}$ and the solid lines are the magnetic filed lines around the rope (LIU et al., 2008).

The initial TD99 flux rope was generated as in (LIU et al., 2008), with a current $I = 7.4 \times 10^{10}$ A. It was set with a major radius (R_f) of $0.14\,R_\odot$, a minor radius $a = 0.026\,R_\odot$, and the center of the magnetic torus below the Sun's surface at $d = 25$ Mm. The GL98 initial flux rope was specified by setting $a = 0.7$, $r_0 = 0.75$, $r_1 = 1.8$, $a_1 = 0.93$, where a is the stretching length of the flux rope into a teardrop shape in the radial direction, r_0 is the flux rope radius, r_1 is the distance from the solar center where the flux rope is placed (prior to the radial contraction) and a_1 is a free parameter that determines the magnetic field strength and plasma pressure in the flux rope.

The choice of such parameters ensures that both CMEs present an equivalent total energy at $2\,R_\odot$, despite their differences on their evolution until there (for example, GL98 takes $\sim$ 4 min to get to $2\,R_\odot$ while TD99 takes $\sim$ 10 min). Moreover, at $2\,R_\odot$, magnetic field strength, density, velocity and pressure are of the same order of magnitude for both models leading us to choose that as the beginning of our analysis. Figure 3.7 show, for comparison, the magnetic field and density at $2\,R_\odot$ for both CMEs.

Within this configuration, the CMEs begin rising right after the flux rope was inserted, as a result of magnetic and thermal pressures. One important aspect that we will focus is the role of the magnetic field configuration in the evolution of the CME. Figure 3.8 presents an isosurface of both CMEs at $2\,R_\odot$.

In the early stages, for both CMEs evolution, it is possible to observe the formation of a shock ahead of them. Figures 3.9a and 3.9b show the refined grid around the CME-driven shock at $t = 10$ min on the x-y plane, for GL98 and TD99, respectively. CMEs were tracked until $6\,R_\odot$ and the effect of both driving mechanisms on their evolution will be presented on Chapter 4.

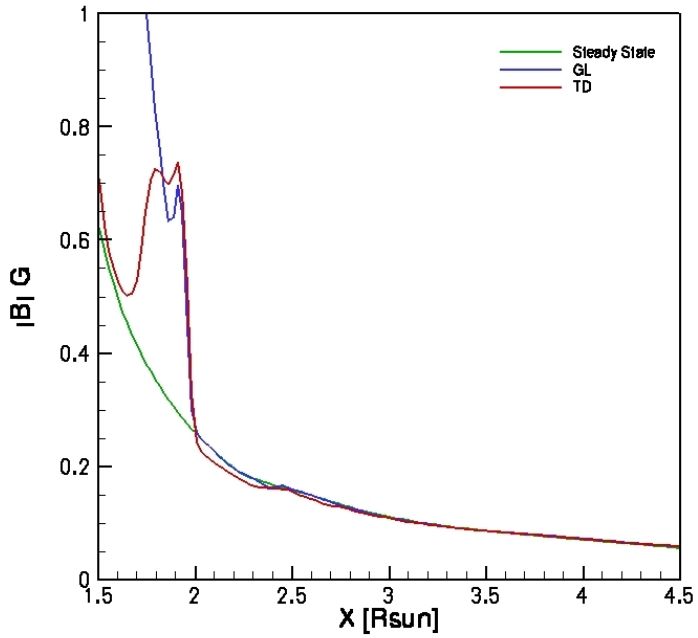

(a)

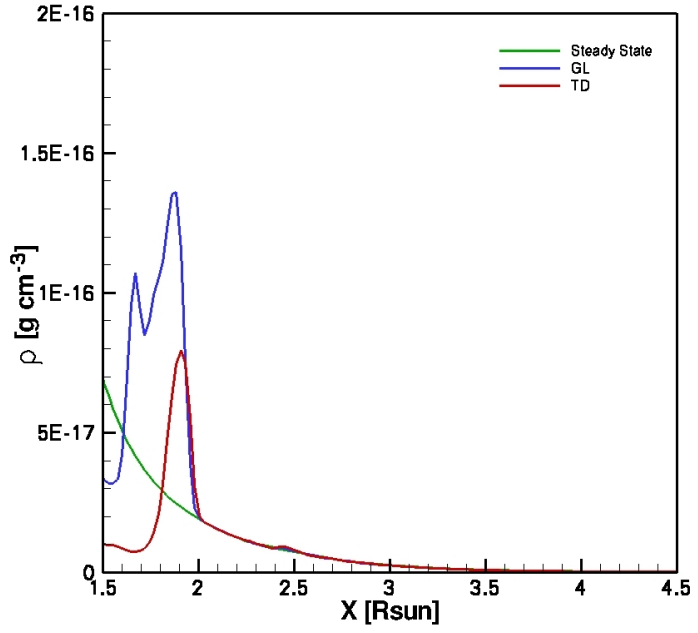

(b)

FIGURE 3.7 - Line plot showing a comparison between the magnetic field strength (a) and the density profile (b) for GL98 (blue line) and TD99 (red line), at a time when the CMEs reached $2\,\mathrm{R}_\odot$: $t \sim 4\,\mathrm{min}$ for GL98 and $t \sim 10\,\mathrm{min}$ for TD99. The green line represents the background solar wind condition before the flux rope is superimposed.

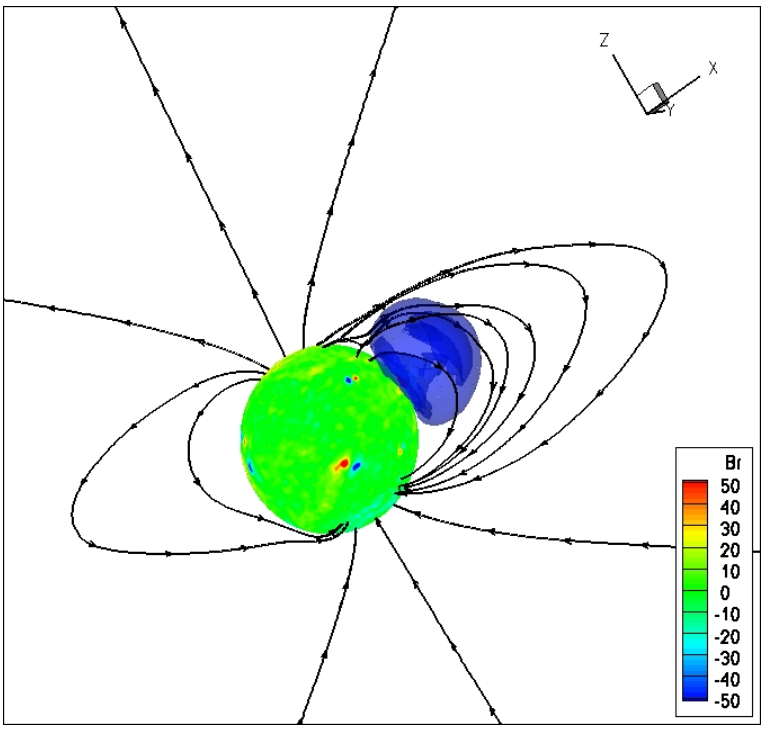

(a)

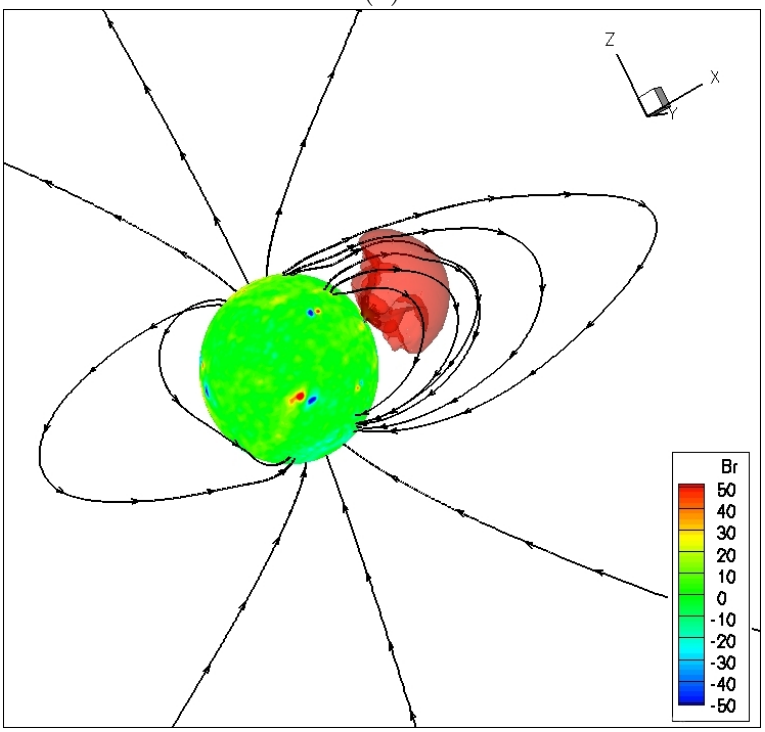

(b)

FIGURE 3.8 - Isosurface of (a) GL98 CME and (b) TD99 CME at $2\,\mathrm{R}_{\odot}$. The spherical surface shows the magnetic field on the solar surface and the black lines represent the Sun's magnetic field lines.

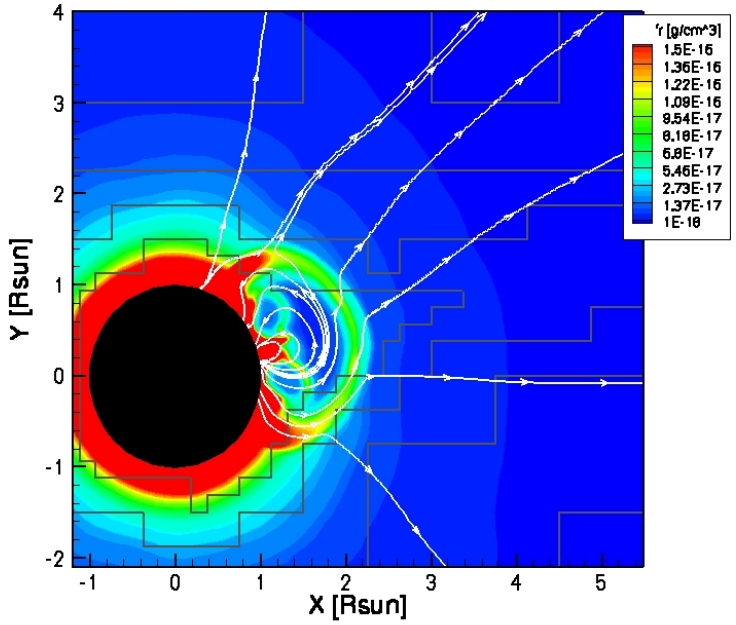

(a)

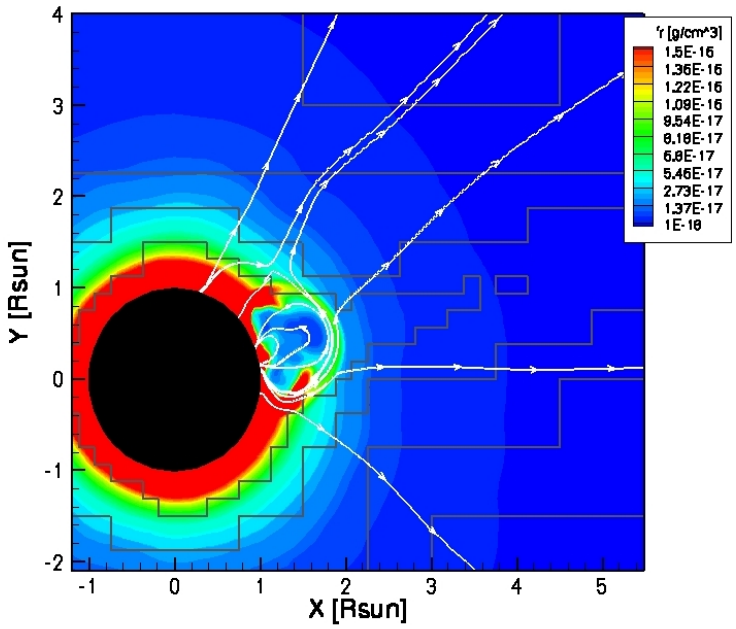

(b)

FIGURE 3.9 - Density contour plot on the lower corona at $t = 10\,\mathrm{min}$ in the x-y plane for a) GL98 and b) TD99. The black lines represent the boundaries of the simulation grid and the white lines represent the magnetic field lines.

4 EVOLUTION OF TWO DIFFERENT CME DRIVING MECHANISMS

The initiation and the early acceleration of CMEs are largely not observed, which sets a major limitation on the understanding of the origin of CMEs and also leads to confusion on the relationship between CMEs and surface phenomena such as flares and filament eruptions (ZHANG et al., 2004). The main objective of this thesis is to explore how different choices of initialization models would affect CME essential features. We have investigated the variation of plasma density, velocity, magnetic field, pressure and drag force along the line going from the center of the Sun to the center of the flux rope (CME's nose). We have also compared the behavior of the driven shock and the CME structure reproduced by both models.

4.1 CME and shock structure

Reproducing the observed structural features of a CME is one of the steps on developing a CME model. A CME observed by a coronagraph usually presents a three part structure defined by a bright frontal loop, a dark cavity and a bright core (HUNDHAUSEN, 1987), as shown in Figure 4.1.

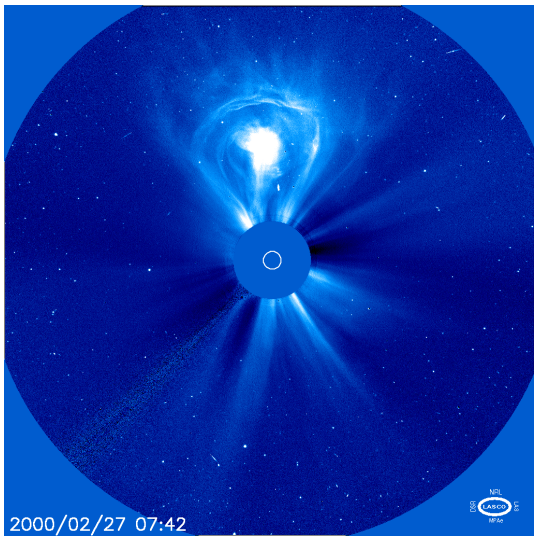

FIGURE 4.1 - A classical three-part CME inside the LASCO C3 field of view, showing a bright frontal loop (shaped as a lightbulb) surrounding a dark cavity with a bright core. The uniform disk in the center of the image is where the occulter is placed, blocking out all direct sunlight. The approximate size of the Sun is indicated by the white circle in the middle.

SOURCE: SOHO (ESA and NASA) (2004)

As described in Chapter 3, in our simulation a CME begins to rise after a flux rope is inserted on top of a steady state background solar wind solution. While propagating away from the Sun, the CMEs reproduce the classical three part structure present in observations. Figure 4.2 shows the CME three part structure at $2\,R_{\odot}$ on the x-y plane, for GL98 and TD99, respectively.

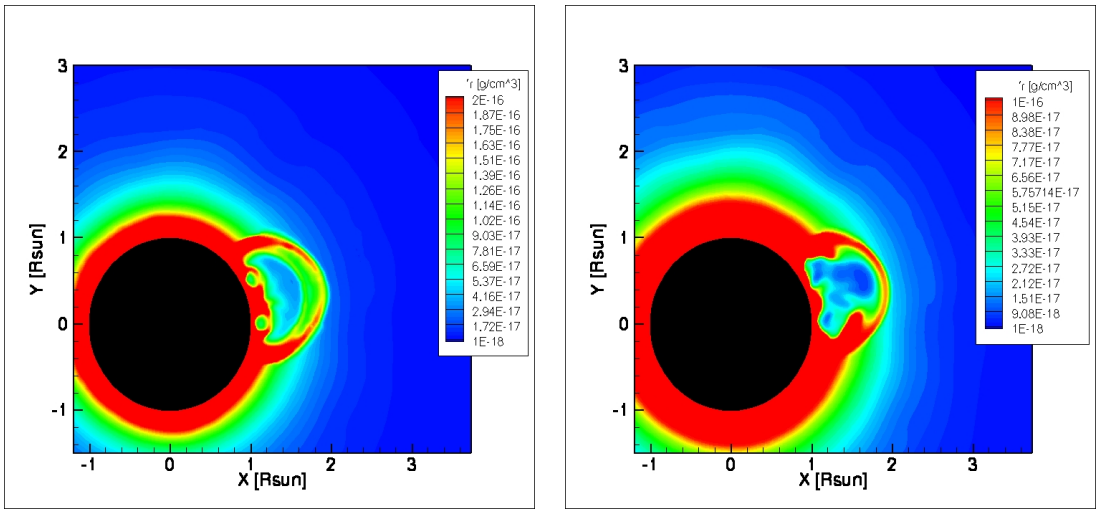

(a) (b)

FIGURE 4.2 - Two-dimensional view of the CME three part structure at $2\,R_{\odot}$ on the x-y plane, (a) GL98 and (b) TD99. The bright frontal loop is the external arc in yellow (red), the dark cavity is represented by the green part between the bright frontal loop and the bright core represented in blue.

As presented in Chapter 3, both CME models used in this thesis propagate through the ambient solar wind, during solar minimum conditions, and it is possible to observe the formation of a shock ahead of them. The ambient SW reproduced by the model presents a bimodal structure with a slow wind in low latitudes and a fast wind flowing on high latitudes. While the CME-driven shock travels, away from the Sun, it interacts with the bimodal SW and distorts its front, forming a dimple. The dimple is an indentation (concave-outward) in the shock front near the current sheet (observed in the x-z plane). The dimple is formed as a result of the difference in speed of the shock in high and low latitudes. As the CME propagates, the indentation in the shock front broadens. Figures 4.3a to 4.3d show the evolution of the dimple in the shock front for GL98 (top panels) and for TD99 (bottom panels), at $2\,R_{\odot}$ ((a) and (c)) and $6\,R_{\odot}$ ((b) and (d)).

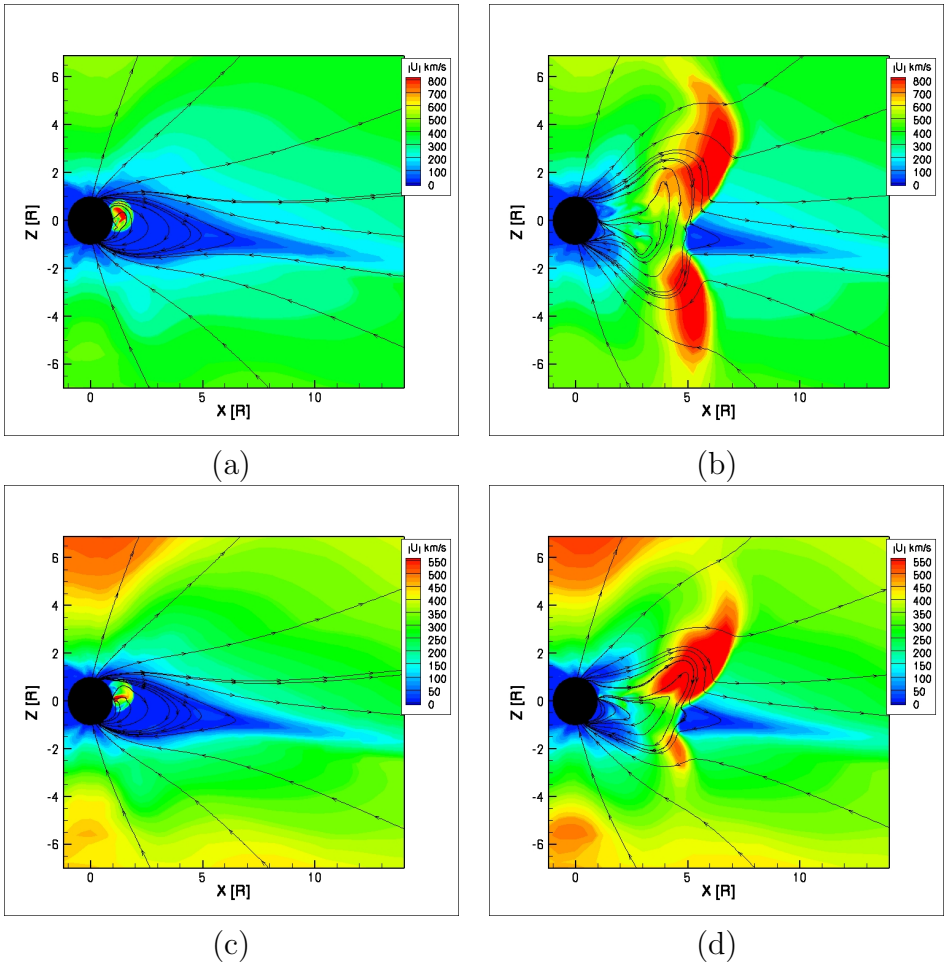

FIGURE 4.3 - Formation of a dimple at the CME front shock on the x-z plane: (a) and (c) represent GL98 and TD99 at $\sim 2\,R_{\odot}$ before the dimple formation, respectively; (b) and (d) represent GL98 and TD99 at $\sim 6\,R_{\odot}$ with a dimple in the shock front, respectively. The black lines represent the magnetic field line.

The formation of the dimple is expected near the current sheet because the shock propagation speed in such region is slower than in higher latitudes, as pointed out by Odstrcil et al. (1996), Tsurutani et al. (2003) and Manchester et al. (2004a) simulations. Manchester et al. (2005) analyzed how flows are deflected at the dimple. They observed an enhancement in the density structure near the dimple and discuss the effect that the dimple has on the post-shock structure and its importance on particle acceleration.

4.2 CME-driven shocks comparison

The study of the origin, the structure, and evolution of CMEs is essential for a deeper insight in space weather physics and prediction (e.g. Le & Han (2005) and Manchester et al. (2005)). A crucial part of it is to understand the formation and strength of the shock close to the Sun. Signatures of shock formation in the corona have been observed in coronagraph images, for fast CMEs. Sime & Hundhausen (1987) observed a bright loop at the front of a CME identified as a coronal shock. Raymond et al. (2000) and Mancuso et al. (2002) reported shocks, observed as type II radio bursts, in the low corona ($R < 3\,\mathrm{R}_\odot$) moving with a speed of $\sim 1000\,\mathrm{km/s}$.

There are evidences that the solar energetic particle (SEP) events associated with CMEs are originated very close to the Sun. It has been proposed that the high energy protons ($> 100\,\mathrm{MeV}$) are produced by an acceleration process at a shock that forms in front of the CME close to the Sun ($< 10\,\mathrm{R}_\odot$) (ROUSSEV et al., 2004). However, how this process occurs is not clear, because of the lack of knowledge about the strength and location of the shock at such an early stage in the evolution of the CME. The prediction of shock properties soon after the onset of the CME requires not only a realistic model of the magnetic field and plasma in the inner corona but also a realistic model of how the CME is initiated (ROUSSEV et al., 2004). In this thesis we analyze how different driving processes of a CME would change the shock evolution characteristics in the lower corona.

We have tracked the CME-driven shocks as they propagate within the lower corona, until $6\,\mathrm{R}_\odot$. We concentrated our comparison near the shock nose, in a region well resolved by the adaptive mesh refinement, defined along the line starting in the center of the Sun going to the center of the flux rope. We focus our analysis on the evolution of four shock characteristic parameters: shock speed, shock compression ratio, Mach number ($\mathrm{M_A}$) and the angle between the shock normal and the upstream magnetic field, θ_{Bn}.

The shock parameters were obtained using theoretical expressions, available in the literature. The speed of the shock was calculated using the Rankine-Hugoniot relation:

$$V_s = \frac{\rho_{up}\mathbf{U}_{up}\cdot\mathbf{n} - \rho_{down}\mathbf{U}_{down}\cdot\mathbf{n}}{\rho_{up} - \rho_{down}} \quad , \tag{4.1}$$

where ρ_{up} ($_{down}$) and $\mathbf{U}_{up}$ ($_{down}$) represent the density and the velocity upstream

(downstream) of the shock respectively, and $\mathbf{n}$ is the shock normal (LUGAZ et al., 2007; LIU et al., 2008).

In Equation 4.1, the shock normal $\mathbf{n}$ was calculated using the velocity coplanarity relation:

$$\mathbf{n} = \frac{\mathbf{U}_{up} - \mathbf{U}_{down}}{\|\mathbf{U}_{up} - \mathbf{U}_{down}\|} \tag{4.2}$$

presented by Kivelson & Russel (1995). $\mathbf{n}$ can also be obtained as a function of the magnetic field ($\mathbf{B}_{up}$ and $\mathbf{B}_{down}$). We use Equation 4.2 to avoid the high variability of magnetic field in downstream side observed in the simulation.

Figure 4.4 shows the results we obtain using Equation 4.1 for GL98 (blue line) and TD99 (red line) models; it also shows the background solar wind speed (black lines). The dashed line in Figure 4.4 represents the background solar wind speed plus 500 km/s. Note that in this chapter in the captions of the figures the models are identified only by GL and TD.

As expected, the plot shows that both CME speeds are faster than the solar wind background. We can also note a small speed decrease in the very initial stage. An explanation for this decrease will be presented in the next section. The shock speed starts to increase around $R = 2.4\,\mathrm{R}_\odot$ in the GL98's case and $R = 2.7\,\mathrm{R}_\odot$ in the TD99's case.

For the GL98 model, the shock speed increases from 650 km/s (at $2.5\,\mathrm{R}_\odot$) to 1040 km/s (at $6\,\mathrm{R}_\odot$). The shock speed for TD99 model ranges from 550 km/s (at $2.5\,\mathrm{R}_\odot$) to 950 km/s (at $6\,\mathrm{R}_\odot$). Figure 4.4 shows that, except for $r < 2.5\,\mathrm{R}_\odot$, GL98 always present a higher shock speed.

Zhang et al. (2004) characterized the CME acceleration considering three parameters: time of duration, magnitude and distance. They have considered three groups: impulsive acceleration events, events with large acceleration ($\sim 300\,\mathrm{m/s^2}$) and a peak speed (> 1000 km/s) that last a short period ($30-50$ min); intermediate acceleration events, with a moderate speed (~ 900 km/s), a moderate acceleration ($\sim 100\,\mathrm{m/s^2}$) and a long duration acceleration $2-3$ hours; and, gradual acceleration events, with a peak speed (~ 350 km/s), a small acceleration ($\sim 4\,\mathrm{m/s^2}$) and a acceleration phase that can last for 24 hours.

For both mechanisms the average shock acceleration is comparable: $\sim 150\,\mathrm{m/s^2}$ for

GL98 and $\sim 100\,\mathrm{m/s^2}$ for TD99 (between $2.3\,\mathrm{R_\odot}$ and $6\,\mathrm{R_\odot}$). If we could compare the results presented here with the selected CME events presented by Zhang et al. (2004), our models can be considered as CMEs with intermediate acceleration.

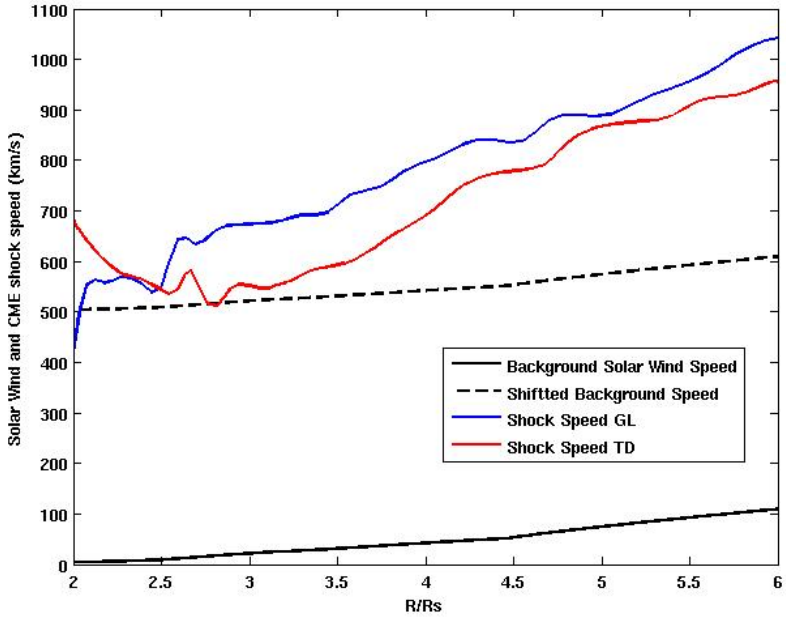

FIGURE 4.4 - Comparison between GL98 (blue line) and TD99 (red line) in terms of their shock speed. The background solar wind speed is shown as a solid black line and the dashed line is the background solar wind speed plus $500\,\mathrm{km/s}$.

We also analyzed the spatial evolution of the fast Mach number (M_A). Figure 4.5 shows the space profile of the fast Mach number for both CME models.

We observe that M_A decreases between $\sim 2.5\,\mathrm{R_\odot}$ and $3.6\,\mathrm{R_\odot}$ (for GL98 from ~ 2.69 to ~ 2.08, and for TD from ~ 2.37 to ~ 1.74) despite the speed increase shown on Figure 4.4. M_A starts to increase for $R > 3.6\,\mathrm{R_\odot}$ for both cases, reaching ~ 2.08 at $5\,\mathrm{R_\odot}$ for GL98, and increasing up to ~ 2.33 at $6\,\mathrm{R_\odot}$. For TD99, M_A increases up to ~ 2.17 at $6\,\mathrm{R_\odot}$. These results indicate a higher compression in the lower corona for the GL98 model, what is an evidence that this model should accelerate particles more efficiently than the TD99 model.

According to θ_{Bn}, shocks can be classified as: perpendicular ($\theta_{Bn} = 90°$); quasi-perpendicular ($45° < \theta_{Bn} < 90°$); parallel $\theta_{Bn} = 0°$; and, quasi-parallel ($0° < \theta_{Bn} <$

45°). In the solar wind none of them prevail and shocks can be found with θ_{Bn} varying from 0° and 90° (PARKS, 1991; BURLAGA, 1995).

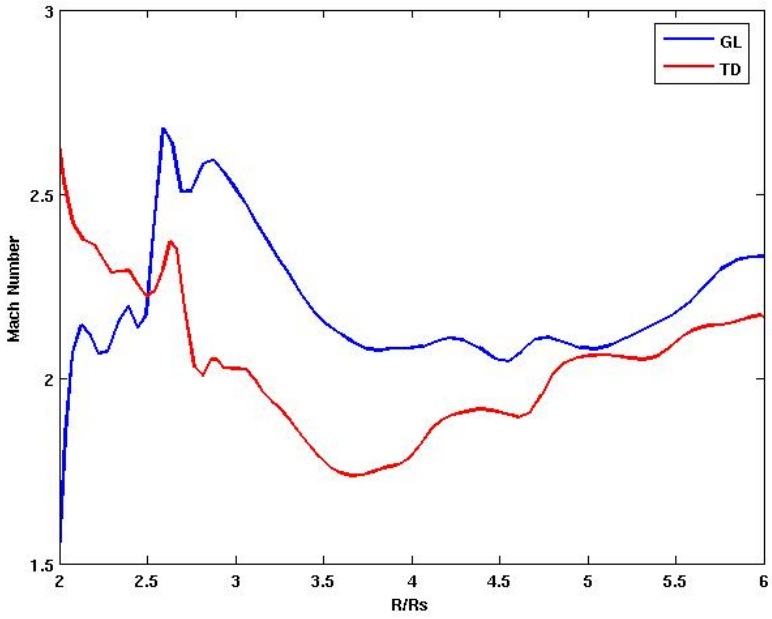

FIGURE 4.5 - Fast Mach Number comparison between GL98 (blue line) and TD99 (red line) vs. the shock position.

In Figure 4.6 we present the θ_{Bn} for both models, showing that the shocks are quasi-parallel at the nose of the CME and there is a decrease of θ_{Bn} while the CME-driven shock is between $2.5\,R_\odot$ and $5\,R_\odot$.

These results are in agreement with the ones presented by Manchester et al. (2005). We can also note that for $r > 5R_\odot$, θ_{Bn} tends to be between 15° and 20° for both models. It is important to mention here that our analyzes is restricted to a region close to the CME nose. Behavior at the flanks can be very different and should be a topic of future investigations.

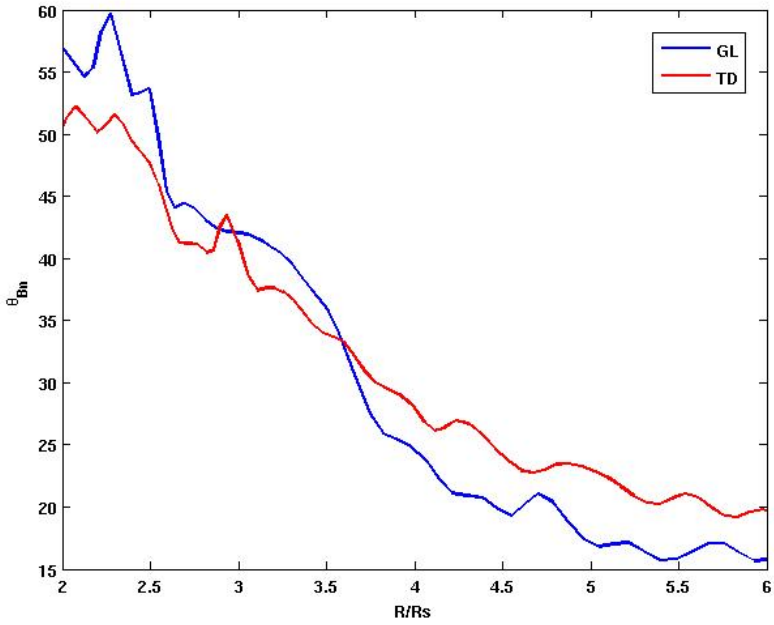

FIGURE 4.6 - Comparison of the angle between the shock normal and the upstream magnetic field θ_{Bn}, for GL98 (blue line) and TD99 (red line).

4.3 CME's sheath and kinematic comparison

While a CME flux rope propagates away from the Sun, a dense plasma is pushed ahead of it, called CME-driven shock. Right behind the shock, between the front shock and the CME, we have the so-called CME sheath.

In the sheath region the solar wind plasma is compressed and the ram pressure increases. Turbulence and temperature anisotropy instabilities can be present in this region, similar to what occur in the Earth magnetosheath (LIU et al., 2006; LIU et al., 2007). CME sheath also presents an enhancement in the density, flow speed, and magnetic field strength (BURLAGA et al., 1981; TSURUTANI et al., 1984; GOSLING, 1993). The turbulence in the sheath, following the shock, is an important ingredient in the acceleration process of energetic particles (LIU et al., 2008).

CME counterparts in the interplanetary space, or ICMEs, are considered geoeffective either because of the presence of strong magnetic fields carried by CMEs, or by the enhancement of an IMF compressed by a CME-driven-shock (BOTHMER; SCHWENN, 1998). It has been shown that the ICME sheaths have an important implication for the generation of geomagnetic storms (LIU et al., 2008). They can bring up to

29% additional energy into the Earth's magnetosphere during geomagnetic storms (ZHANG et al., 2008). Observations have also shown that the sheath region can be as geoeffective as the ICME themselves (TSURUTANI et al., 1988).

In this work we investigate the kinematics of the CME just in the sheath region since the flux rope region is resolved with less accuracy them the sheath region. The region near the flux rope is dominated by reconnection and will be considered in future studies.

To determine the CME sheath limits we first define the upstream and downstream limits. The sheath upstream limit is defined as the shock position obtained from the CME velocity profile. The shock position is the average position between the blue line and red line limits shown on Figure 4.7a. In Figure 4.7a the inclination between the blue and the red line is due to numerical resolution. The sheath's downstream limit is defined as the first peak of the density profile behind the shock (found as the first maximum of the spatial derivative of the density). Knowing the shock position, extracted from the velocity profile, we consider this position on the density profile. The first maximum of the spatial derivative of the density behind the shock is the sheath downstream limit. Figure 4.7b shows the density profile with the indication of the sheath upstream (blue line) and downstream (red line) limits.

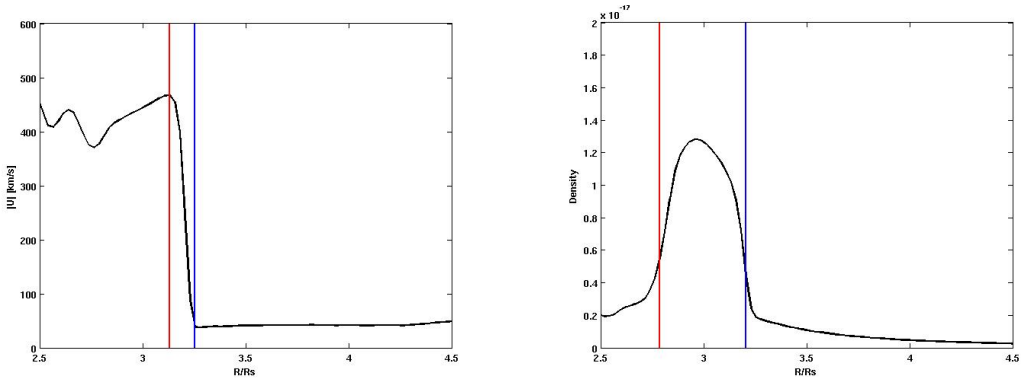

(a) (b)

FIGURE 4.7 - CME's shock and sheath's regions. a) shock position calculated from the velocity profile. The shock position is determined as the average point between the blue and the red lines. b) sheath upstream (blue line) and downstream (red line) limits calculated from the density profile. Results for TD99 model.

CMEs expand with the distance from the Sun and the same happens to the sheaths that increase in size. The sheath for interplanetary counterparts of CMEs (ICMEs) also increase their scale from $\sim$ 0.01 AU near the Sun to tens of AU after the termination shock (location in the heliosphere where the SW becomes subsonic, due to the interaction with the interstellar medium)(RICHARDSON; LIU, 2007). Figure 4.8 shows the spatial evolution of the CME sheath for GL98 and TD99 models.

The expansion of the sheath is observed for both models, except for a small region near the Sun, between 2 $R_\odot$ and 2.5 $R_\odot$ for the GL98 model. The rate of expansion is similar for both models, between 2.5 $R_\odot$ and 4.8 $R_\odot$. After that expansion rate for GL98 stays the same, while for TD99 it slows down. At 6 $R_\odot$, for the GL98 model, the sheath width is $\sim$ 1.89 $R_\odot$ while for TD99 it is $\sim$ 1.59 $R_\odot$.

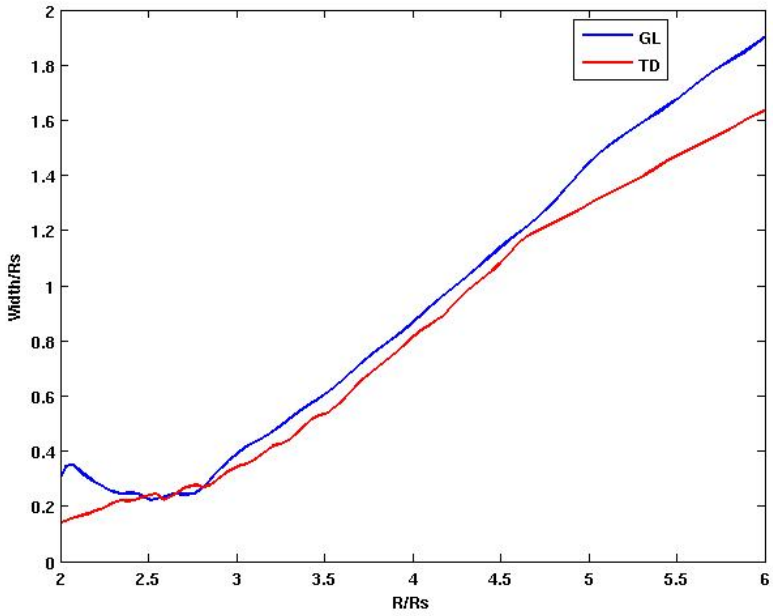

FIGURE 4.8 - Space profile for the width of the CME sheath for both driving mechanisms: GL98 (blue line) and TD99 (red line).

One of the key aspects on understanding CME's kinematic processes is the acceleration profile. The CME acceleration "a" is given by :

$$(M_{CME} + V_M) \cdot a = F_G + (P_{low} + P_{up}) \cdot area - F_D, \tag{4.3}$$

where, M_{CME} is the CME mass, V_M the virtual mass, P_{low} denotes magnetic and thermal pressure on the lower surface area, P_{up} denotes the same quantities on the upper surface area, F_G is the gravitational force and F_D is the drag force (FORBES et al., 2006). The virtual mass V_M is a concept from hydrodynamics related to the force needed to move away the ambient medium, as a body is accelerated in a fluid. In our case the apropriate increase in the mass of the body V_M is obtained by its width and density ratio.

While moving away from the Sun, a CME experiences a drag force that tries to decelerate it. The standard drag term (F_D) is given by:

$$F_D = C_D \cdot A \cdot \rho |V_{CME} - V_{SW}|(V_{CME} - V_{SW}) \quad , \tag{4.4}$$

where A is the cross-sectional area of the body, $V_{CME} - V_{SW}$ is the relative velocity between the CME and the solar wind, and C_D is the drag coefficient (FORBES et al., 2006). While in non-magnetized fluids $C_D = 1$, in magnetized fluids the drag coefficient is considered smaller $C_D < 1$, because when flowing around a magnetized body, the plasma is constrained by the magnetic field. Since the drag force seems to be smaller in a low-β plasma than in a high-β plasma, C_D can be also set as a $\tanh \beta$, where β is the ratio of plasma pressure and magnetic pressure (CARGILL et al., 1996).

In Figures 4.9a and 4.9b we show the modeled CME acceleration for GL98 and TD99, respectively, and the four theoretical predicted accelerations for each case.

The four cases are the limiting cases where $C_D \sim 1$ or $\tanh \beta$ with and without V_M. The results show a good qualitative match between the general profile of the modeled acceleration and the four predictions for GL98 and TD99. Forbes et al. (2006) pointed out that the virtual mass V_M is negligible for $R > 1.5\,\mathrm{R}_\odot$. Results presented here agree with this statement since V_M seems to play no role on modifying the CMEs acceleration profile after $1.5\,\mathrm{R}_\odot$, for both models. However, GL98's modeled acceleration behavior do not seems to match none of the four predictions. TD99's modeled acceleration presents a better match with our four prediction profiles, but its large fluctuating profile does not allow us to be sensitive to which prediction is better for the whole range. TD99 seems to be better fitted with $C_D \sim \tanh \beta$ after $4\,\mathrm{R}_\odot$.

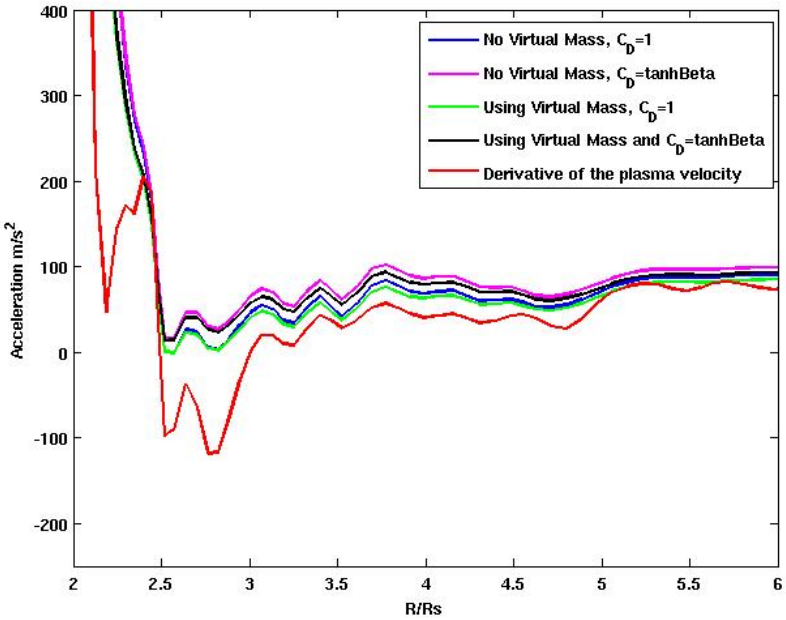

(a)

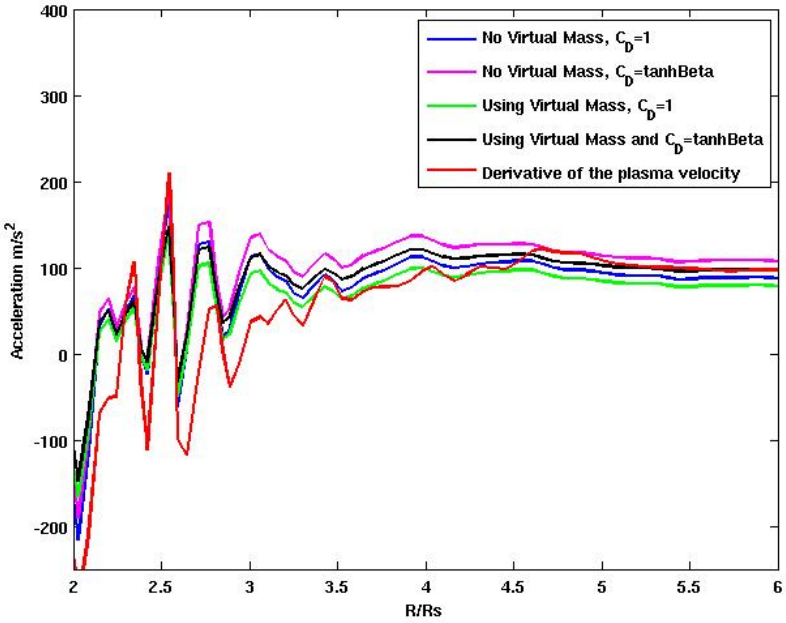

(b)

FIGURE 4.9 - Comparison between the predicted acceleration profiles using $C_D \sim 1$ and $V_M = 0$ (blue line); $C_D \sim 1$ and $V_M \neq 0$ (green line); $C_D \sim \tanh\beta$ and $V_M = 0$ (pink line); $C_D \sim \tanh\beta$ and $V_M \neq 0$ (black line) for the sheath and the modeled acceleration (red line) for both driving models: a) GL98; b) TD99.

The magnetic and thermal pressure profile within the sheath region, their sum and the force of drag and gravity forces profile are shown on Figures 4.10a and 4.10b for GL98 and TD99, respectively.

Analyzing the forces shown in Figures 4.10a and 4.10b we observe that the magnetic pressure plays an important role in both cases, contributing for the CME acceleration. This contribution in GL98's case is important until $\sim 4\,R_\odot$, where the thermal pressure begins to dominate. In the case of TD99 model, the magnetic pressure contribution to the acceleration extends only to $R \leq 3\,R_\odot$. It also shows that GL98 has enough total pressure (magnetic plus thermal) to overcome the drag force and gravity, until $\sim 4\,R_\odot$. On the other hand, for TD99 the total pressure overcomes the drag force and gravity only until $\sim 2.5\,R_\odot$, and gravity does not seem to have a contribution as strong as in GL98's. Figures 4.11a and 4.11b show, for GL98 and TD99 respectively, the magnetic and thermal pressure profile, their sum and the drag and gravity forces profile in a log scale, for better visualization of the results presented.

These results show that the magnetic field is very important in the early stages of the CME propagation process for both acceleration mechanisms, being more efficient in GL98's case. However, while in the GL98 case the CME is driven by a combination of magnetic and thermal pressure, in the TD99 the thermal pressure dominates the evolution. This issue will be addressed when we present our conclusion on Chapter 5.

Another physical process related to CMEs that is an important aspect of space weather models is the acceleration of solar energetic particles (SEPs) in CME-driven shocks. SEPs can be accelerated within a short time after the CME initiation. Since very little is know about CME-driven shocks soon after the onset of the eruption, many theories about the acceleration process have been discussed (e.g., Tylka (2001); Reames (2002)).

Manchester et al. (2005) discuss the existence of a compression in the SW plasma behind the shock, the so-called post-shock compression. The post-shock compression was found as a density and field strength increase behind the shock and was observed between $6\,R_\odot$ and $20\,R_\odot$, within CMEs with speeds $> 1000\,km/s$. This post shock compression may generate instabilities to accelerate particles.

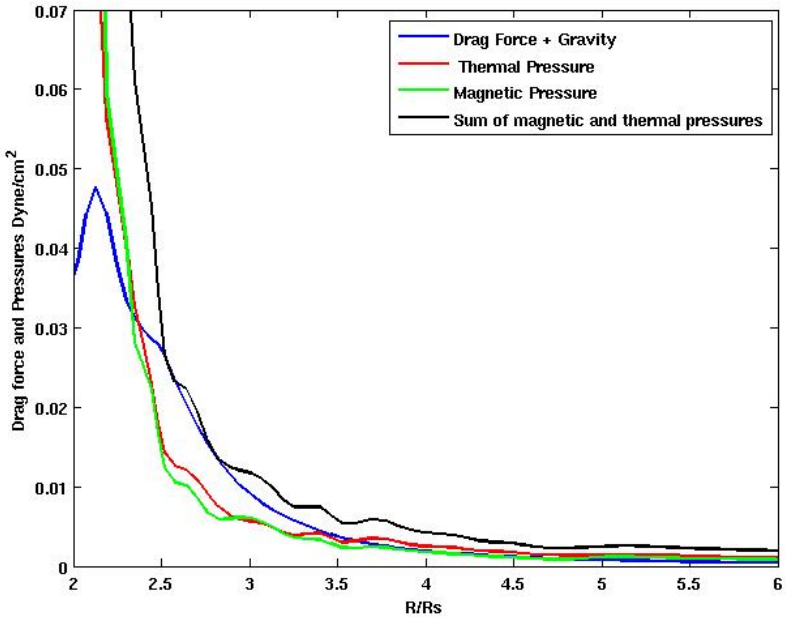

(a)

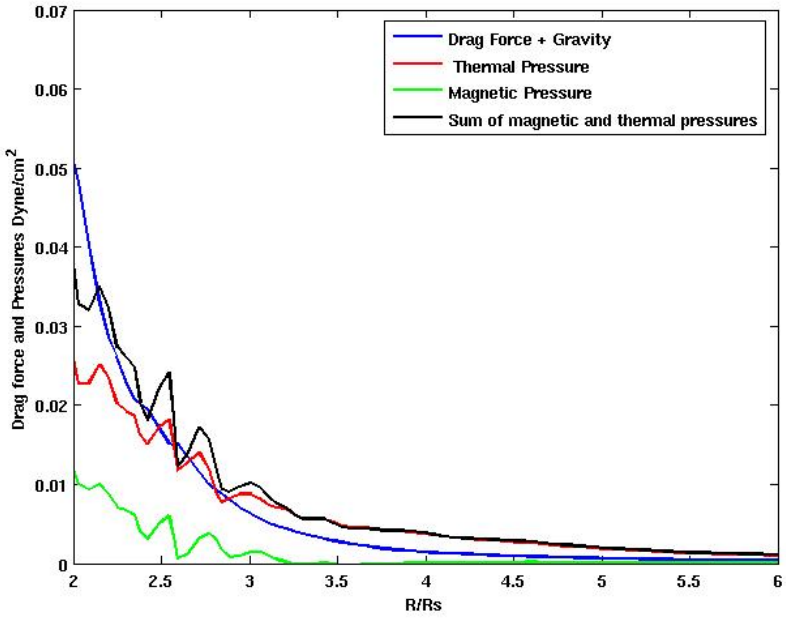

(b)

FIGURE 4.10 - Drag force (blue line) and pressures profiles for both GL98 (a) and TD99 (b), calculated in the sheath of both CMEs. The pressure profiles include the magnetic pressure (green line), the thermal pressure (red line) and their sum (black line).

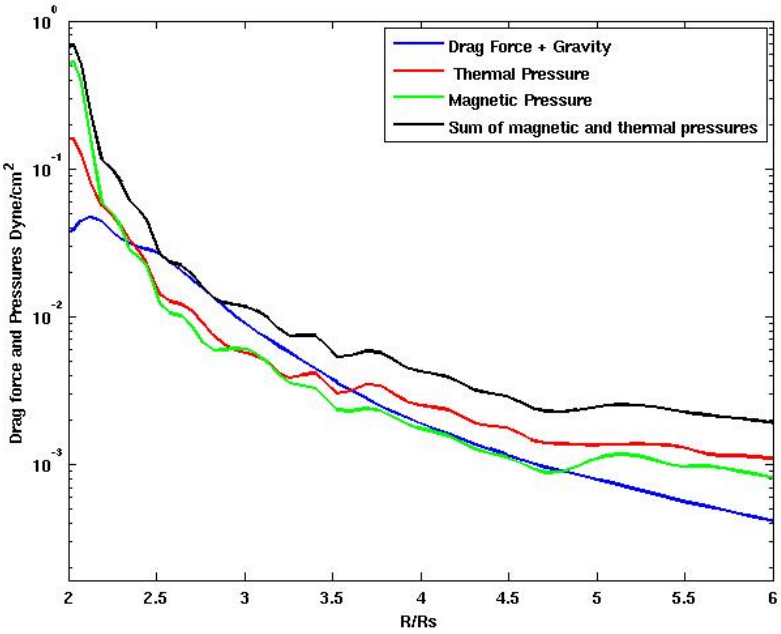

(a)

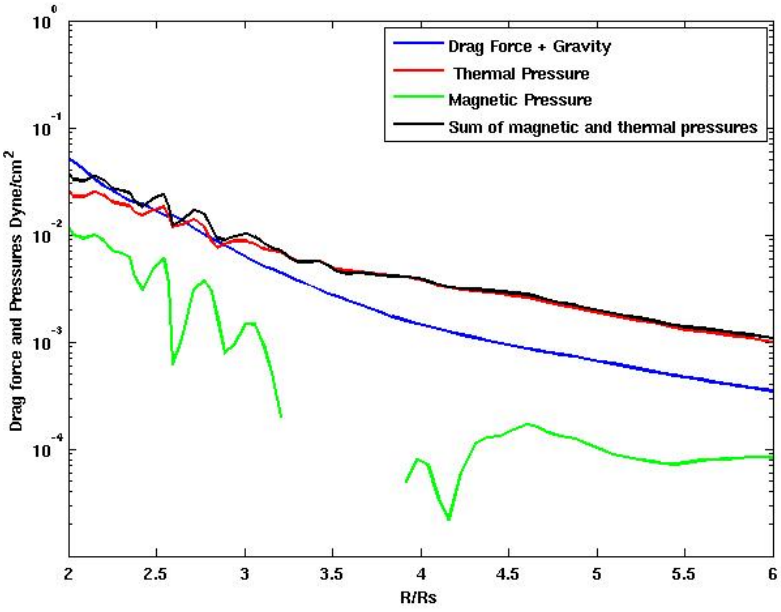

(b)

FIGURE 4.11 - Drag force (blue line) and pressures profiles for both GL98 (a) and TD99 (b), calculated in the sheath of both CMEs and presented in a log scale. The pressure profiles include the magnetic pressure (green line), the thermal pressure (red line) and their sum (black line).

Liu et al. (2008) described, besides the shock, a plasma compression from immediately downstream to further downstream, with a maximum density at about 4 times the density just downstream of the shock, for a TD99 CME simulation, as show in Figure 4.12.

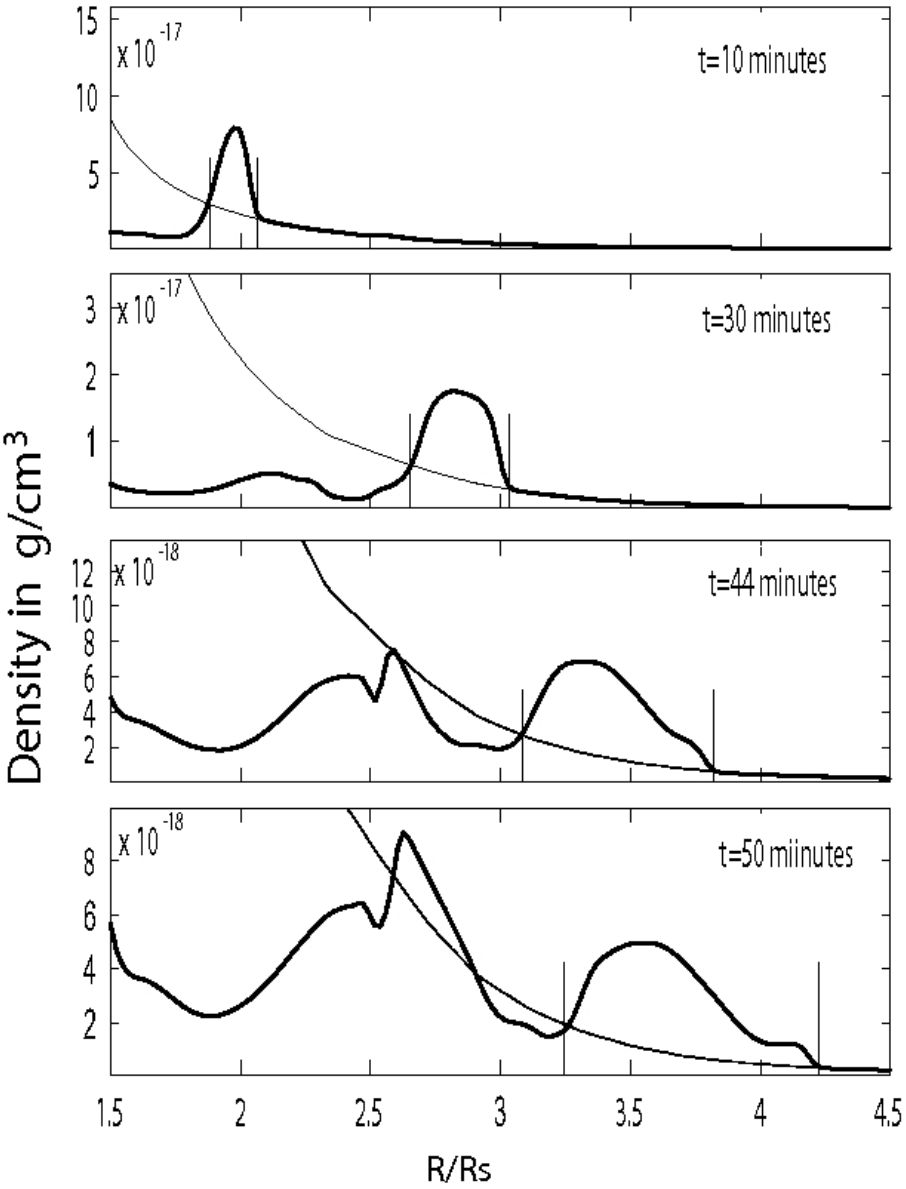

FIGURE 4.12 - Plasma density behind the TD99 CME-driven shock versus distance at time t=10, 30, 44, 50 minutes (thick curves) and for the steady state solar wind (thin line).

SOURCE: Liu et al. (2008)

In our simulations, we have observed that both CME acceleration mechanisms presented more than a shock jump compressing the plasma. A compression was also seen further downstream for $R > 2.5\,\mathrm{R}_{\odot}$. Such compression is known as post-shock compression. Figure 4.13 shows both the shock and the post-shock compression ratio, where the post-shock compression ratio is defined as the maximum density of the secondary, downstream enhancement divided by the density immediately downstream.

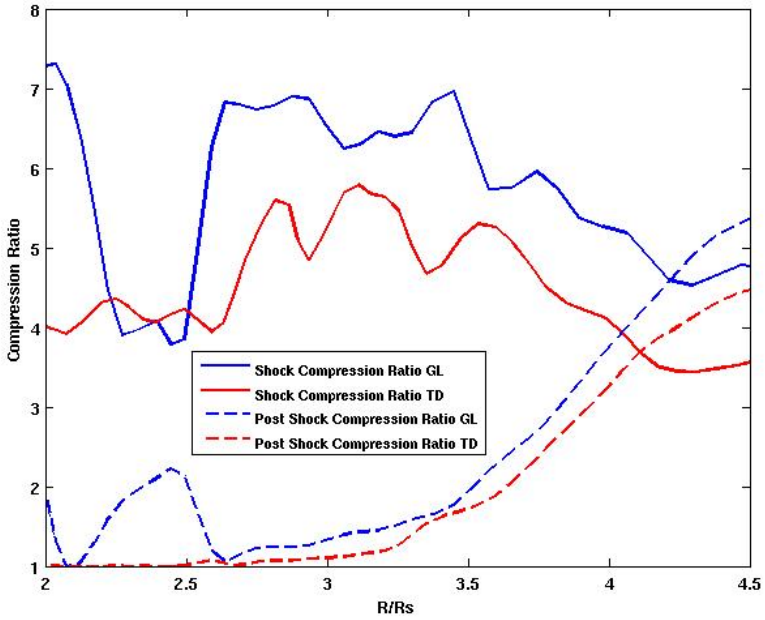

FIGURE 4.13 - Shock and post-shock compression ratio vs. the shock position. The shock (solid lines) and the post-shock (dashed lines) compression are shown in blue for GL98 and in red for TD99.

In Figure 4.13 we observe that the post-shock compression is slightly larger for GL98 CME than for TD99. And that it tends to increase as the CME propagates away from the Sun.

5 CONCLUSION

Coronal mass ejections are large expulsions of coronal plasma into the interplanetary space. Understanding their behavior and the effects of their interaction with the solar wind within hours or days before they get to Earth is one of the goals of space weather research.

In this work we present a comparison of a 3D simulation of CMEs, in the lower corona, generated with two different mechanisms: GL98 and TD99. We investigated the CME shock evolution and kinematics, focusing on comprehending how the initial magnetic configuration of a CME changes its evolution through the lower corona, between $2\,R_\odot$ and $6\,R_\odot$.

Both models describe a self-similar solution of a CME propagation outwards the corona, reproducing their classical three-part structure usually present in observations: bright frontal, dark cavity and bright core. They also show the formation of a dimple on the CME-driven shock front near the current sheet region, which results from its interaction with the bimodal solar wind.

The CME-driven shock generated for both models are quasi-parallel at the nose and the angle between the shock normal and the upstream magnetic field (θ_{Bn}) decreases with its distance from the Sun, in agreement with Manchester et al. (2005). For distances larger then $6\,R_\odot$, θ_{Bn} tends to stay between 15° and 20°.

As expected, the CME shock speeds are faster than the solar wind background. They present a small speed decrease (deceleration) in the very initial stage. Such decrease in the shock speed can be associated to the fact that the combination of drag force and gravity, in this stage of the CME evolution, is larger than the total pressure, and holds the CME evolution. After the total pressure overcomes the combination of drag force and gravity (around $2.5\,R_\odot$) the CME speed increases up to $950 - 1040\,km/s$. We also observed that within the region of interest in this thesis, $2.3\,R_\odot$ to $6\,R_\odot$, GL98 acceleration is higher $\sim 150\,m/s^2$, when compared to $\sim 100\,m/s^2$ for TD99.

The Mach number decreases between $2.5\,R_\odot$ and $3.6\,R_\odot$, increasing after that for both models, with M_A for GL98 being larger than for TD99, for $R > 2.5\,R_\odot$. These results indicate a higher compression for GL98 in the lower corona, implying that it should accelerate particles more efficiently than the TD99 model.

It is observed that the expansion rate of the sheath is similar, between $2.5\,R_\odot$ and $4.8\,R_\odot$, for both models. However, after that distance, the sheath dimension is larger for GL98, being $\sim 1.89\,R_\odot$ (at $6\,R_\odot$) while for TD99 it is $\sim 1.59\,R_\odot$.

We also have observed, as discussed in Manchester et al. (2005), the existence of a post-shock compression after $\sim 2.5\,R_\odot$ for both models. Such compression was slightly larger for the GL98 model, tending to increase within the distance from the Sun for both models.

Our results show that both our models present a quasi-parallel shock with a higher compression in GL98 case. They both also presented a post-shock compression that tends to increase within the distance from the Sun. The GL98 model presents a faster shock speed and a higher M_A, an indication of higher compression in the lower corona, and implying that for this model the particle acceleration can be more efficient than for TD99. We also find that the sheath in the GL98 model has a slightly larger expansion. Despite their differences, our results show a tendency of both CMEs to have similar behavior after $6\,R_\odot$. The results obtained in this thesis indicate that understanding the role of magnetic fields in the initiation of CMEs is a crucial issue to study the CME evolution close to the Sun. And that the differentiation between distinct initiation mechanisms most likely will be observed very close to the Sun.

Understanding how the flux tube and the solar wind total pressure behaves during the early stages, could tell us some important differences between the acceleration mechanisms, depending on the forces acting in the process. Our results for the dependence on thermal and magnetic pressures, and drag and gravity forces for the CME acceleration confirm the results presented by Forbes et al. (2006): the virtual mass is negligible for $r > 1.5\,R_\odot$ for both models. Analyzing the acceleration profiles we observe that the TD99 presents a better match with $C_D \sim \tanh\beta$ at $r > 4\,R_\odot$, a good approximation for low beta plasmas. We also observe that the magnetic pressure plays an important role in both cases, contributing to the CME evolution. We concluded that what drives the CME sheath evolution in GL98 model is a combination of magnetic and thermal pressure, until $6\,R_\odot$, confirming what has been previously observed by Manchester et al. (2004a). Similar result was expected to be found using TD99. However, our results show that the thermal pressure dominates the evolution all the way to $6\,R_\odot$ in the case of TD99.

Investigating the reasons for these findings, we looked for different behavior between

the models. We found that the sheath average mass for GL98 is approximately 20% larger than for TD99. We have also observed that in the flanck regions of the CMEs the plasma accelerates very rapidly, faster than the ambient solar wind (see Figure 4.3). An extra acceleration also seem to happen immediately behind the shock. An increase in the CME temperature within the distance from the Sun has been also noted.

We believe that this anomalous acceleration and heating can be related to the variable polytropic index distribution used on the steady state solar wind simulation. The variable γ could be changing after the CME is inserted. Such variable γ could be inserting additional heating into the background or be adding thermal energy to the CME while it is evolving through the lower corona.

Since our results are confined along a line going from the center of the Sun to the center of the flux rope (CME's nose) within the lower corona, we can not be sure if the problem is numerical or physical. Increasing the grid refinement in the disturbed regions and setting the γ to be fixed in its original profile once the CME is initiated are two of the options to analyze this issue. We are currently investigating this anomalous heating and acceleration.

Our work intends to be a prototype of the differences among intermediated speed CMEs in the lower corona. Here we are looking forward to comprehend how the CME signatures would change in the lower corona for CMEs accelerated by different mechanisms, specially before $6\,R_\odot$. Our results show that after $6\,R_\odot$ both CME models tend to propagate similarly. The importance of this kind of study is reinforced by the fact that most studies on CMEs are based on observations that are performed usually above $10\,R_\odot$ and closer to the Earth. Emphasizing the fact that the initiation and the early acceleration of CMEs are largely not observed and increasing the importance of CME models and simulation within the lower corona region. The benchmark of the models is done considering the most close observations available in the literature.

REFERENCES

ALTSCHULER, M. D.; NEWKIRK, G. Magnetic fields and the structure of the solar corona. I: methods of calculating coronal fields. **Solar Physics**, v. 9, n. 1, p. 131–149, sep. 1969. 44, 46

ANTIOCHOS, S. K.; DEVORE, C. R.; KLIMCHUK, J. A. A model for solar coronal mass ejections. **The Astrophysical Journal**, v. 510, n. 1, p. 485–493, jan. 1999. 24, 25, 28

ARGE, C. N.; LUHMANN, J. G.; ODSTRCIL, D.; SCHRIJVER, C. J.; LI, Y. Stream structure and coronal sources of the solar wind during the May 12th, 1997 CME. **Journal of Atmospheric and Solar-Terrestrial Physics**, v. 66, n. 15-16, p. 1295–1309, oct. 2004. 44, 45

ARGE, C. N.; PIZZO, V. J. Historical verification of the Wang-Sheeley model: further improvements in basic technique. In: SOLAR WIND NINE CONFERENCE, 9., 1998, Nantucket, United States of America. **Proceedings...** Nantucket, MA: AIP Conference Proceedings, 1999. p. 569–572. 46

_____. Improvement in the prediction of solar wind conditions using near-real time solar magnetic field updates. **Journal of Geophysical Research**, v. 105, n. A5, p. 10465–10480, may 2000. 44

BOTHMER, V.; SCHWENN, R. The structure and origin of magnetic clouds in the solar wind. **Annales Geophysicae**, v. 16, n. 1, p. 1–24, 1998. 60

BURLAGA, L.; SITTLER, E.; MARIANI, F.; SCHWENN, R. Magnetic loop behind an interplanetary shock - Voyager, Helios, and IMP-8 observations. **Journal of Geophysical Research**, v. 68, p. 6673–6684, aug. 1981. 60

BURLAGA, L. F.; PLUNKETT, S. P.; CYR, O. C. S. Successive CMEs and complex ejecta. **Journal of Geophysical Research**, v. 107, n. A10, p. SSH 1–1, oct. 2002. 24

BURLAGA, L. F. E. **Physics of the inner heliosphere II. Particles, waves and turbulence**: magnetic clouds. Berlin: Springer-Verlag, 1991. 352 p. 24

_____. **Interplanetary magnetohidrodynamics**. New York: Oxford University Press, 1995. 538 p. 59

CARGILL, P. J.; CHEN, J.; SPICER, D. S.; ZALESAK, S. T. Magnetohydrodynamic simulations of the motion of magnetic flux tubes through a magnetized plasma. **Journal of Geophysical Research**, v. 101, n. A3, p. 4855–4870, mar. 1996. 63

CHEN, J. Theory of prominence eruption and propagation: interplanetary consequences. **Journal of Geophysical Research**, v. 101, n. A12, p. 27499–27520, dec. 1996. 28

COHEN, O.; SOKOLOV, I. V.; ROUSSEV, I. I.; ARGE, C. N.; MANCHESTER, W. B.; GOMBOSI, T. I.; FRAZIN, R. A.; PARK, H.; BUTALA, M. D.; KAMALABADI, F.; VELLI, M. A semiempirical magnetohydrodynamical model of the solar wind. **The Astrophysical Journal**, v. 654, n. 2, p. L163–L166, jan. 2007. 27, 31, 41, 44, 46

COHEN, O.; SOKOLOV, I. V.; ROUSSEV, I. I.; GOMBOSI, T. I. Validation of a synoptic solar wind model. **Journal of Geophysical Research**, v. 113, n. A3, mar. 2008. 44, 46

EVANS, R. M.; OPHER, M.; MANCHESTER, W. B.; GOMBOSI, T. I. Alfvén profile in the lower corona: implications for shock formation. **The Astrophysical Journal**, v. 687, n. 2, p. 1355–1362, nov. 2008. 43

FORBES, T. G.; LINKER, J. A.; CHEN, J.; CID, C.; KÓTA, J.; LEE, M. A.; MANN, G.; MIKIĆ, Z.; POTGIETER, M. S.; SCHMIDT, J. M.; SISCOE, G. L.; VAINIO, R.; ANTIOCHOS, S. K.; RILEY, P. CME theory and models. **Space Science Reviews**, v. 123, n. 1-3, p. 251–302, mar. 2006. 27, 33, 63, 72

FORBES, T. G.; PRIEST, E. R. Photospheric magnetic field evolution and eruptive flares. **The Astrophysical Journal**, v. 446, p. 377, jun. 1995. 25, 28

GIBSON, S. E.; LOW, B. C. A time-dependent three-dimensional magnetohydrodynamic model of the coronal mass ejection. **The Astrophysical Journal**, v. 493, p. 460 – 473, jan. 1998. 17, 24, 25, 28, 32, 33, 34, 48

GOSLING, J. T. The solar flare myth. **Journal of Geophysical Research**, v. 98, n. A11, p. 18937–18950, nov. 1993. 23, 60

GROTH, C. P. T.; ZEEUW, D. L. D.; GOMBOSI, T. I.; POWELL, K. G. Global three-dimensional MHD simulation of a space weather event: CME formation,

interplanetary propagation, and interaction with the magnetosphere. **Journal of Geophysical Research**, v. 105, n. A11, p. 25053–25078, nov. 2000. 27, 29, 31, 42, 47

HOEKSEMA, J. T.; WILCOX, J. M.; SCHERRER, P. H. Structure of the heliospheric current sheet in the early portion of sunspot cycle 21. **Journal of Geophysical Research**, v. 87, p. 10331–10338, dec. 1982. 45

HOLST, B. van der; JACOBS, C.; POEDTS, S. Simulation of a breakout coronal mass ejection in the solar wind. **The Astrophysical Journal**, v. 671, n. 1, p. L77–L80, dec. 2007. 28, 33

HUNDHAUSEN, A. J. The origin and propagation of coronal mass ejections. In: INTERNATIONAL SOLAR WIND CONFERENCE, 6., 1987, Estes Park, United States of America. **Proceedings...** Estes Park, CO: NCAR Technical Note NCAR/TN-306+Proc, 1987. v. 2, p. 181. 25, 33, 53

_____. Sizes and locations of coronal mass ejections - SMM observations from 1980 and 1984-1989. **Journal of Geophysical Research**, v. 98, n. A8, p. 13,177–13,200, aug. 1993. 35

_____. An introduction. In: CROOKER, N.; JOSELYN, J.; FEYMAN, J. (Ed.). **Coronal mass ejections**. [S.l.]: AGU, Washington, DC, 1997. p. 01–07. 23

HUNDHAUSEN, A. J.; SAWYER, C. B.; HOUSE, L.; ILLING, R. M. E.; WAGNER, W. J. Coronal mass ejections observed during the solar maximum mission - latitude distribution and rate of occurrence. **Journal of Geophysical Research**, v. 89, p. 2639–2646, 1984. 23

KIVELSON, M. G.; RUSSEL, C. T. **Introduction to space physics**. New York: Cambridge University Press, 1995. 568 p. 19, 20, 22, 57

KUZNETSOVA, M. M.; HESSE, M.; RASTATTER, L.; TAKTAKISHVILI, A.; TOTH, G.; ZEEUW, D. L. D.; RIDLEY, A.; GOMBOSI, T. I. Multiscale modeling of magnetospheric reconnection. **Journal of Geophysical Research**, v. 112, n. A10, oct. 27

LE, G. M.; HAN, Y. B. Analysis of the acceleration process of SEPs by an interplanetary shock for bastille day event. In: CORONAL AND STELLAR MASS EJECTION, IAU SYMPOSIUM, 226., 2004, Beijing, China. **Proceedings...** Beijing: Cambridge University Press, 2005. p. 346–349. 56

LINKER, J. A.; MIKIĆ, Z. Disruption of a helmet streamer by photospheric shear. **The Astrophysical Journal**, v. 438, n. 1, p. L45–L48, jan. 1995. 25, 27, 28

LINKER, J. A.; MIKIĆ, Z.; BIESECKER, D. A.; FORSYTH, R. J.; GIBSON, S. E.; LAZARUS, A. J.; LECINSKI, A.; RILEY, P.; SZABO, A.; THOMPSON, B. J. Magnetohydrodynamic modeling of the solar corona during whole Sun month. **Journal of Geophysical Research**, v. 104, n. A5, p. 9809–9830, may 1999. 27

LITES, B. W.; LOW, B. C.; PILLET, V. M.; SEAGRAVES, P.; SKUMANICH, A.; FRANK, Z. A.; SHINE, R. A.; TSUNETA, S. The possible ascent of a closed magnetic system through the photosphere. **The Astrophysical Journal**, v. 446, p. 877, jun. 1995. 33

LIU, Y.; MANCHESTER, W. B.; RICHARDSON, J. D.; LUHMANN, J. G.; LIN, R. P.; BALE, S. D. Deflection flows ahead of ICMEs as an indicator of curvature and geoeffectiveness. **Journal of Geophysical Research**, v. 113, n. 13, jul. 2008. 60

LIU, Y.; RICHARDSON, J. D.; BELCHER, J. W.; KASPER, J. C.; SKOUG, R. M. Plasma depletion and mirror waves ahead of interplanetary coronal mass ejections. **Journal of Geophysical Research**, v. 111, n. A9, sep. 2006. 60

LIU, Y.; RICHARDSON, J. D.; BELCHER, J. W.; KASPER, J. C. Temperature anisotropy in a shocked plasma: mirror-mode instabilities in the heliosheath. **The Astrophysical Journal**, v. 659, n. 1, p. L65–L68, apr. 2007. 60

LIU, Y. C.-M.; OPHER, M.; COHEN, O.; LIEWER, P. C.; GOMBOSI, T. I. A simulation of a coronal mass ejection propagation and shock evolution in the lower solar corona. **The Astrophysical Journal**, v. 680, n. 1, p. 757–763, jun. 2008. 25, 28, 33, 38, 44, 48, 49, 57, 68

LUGAZ, N.; MANCHESTER W. B., I.; GOMBOSI, T. Numerical simulation of the interaction of two coronal mass ejections from Sun to Earth. **The Astrophysical Journal**, v. 634, n. 1, p. 651–662, nov. 2005b. 25, 27, 28, 33

LUGAZ, N.; MANCHESTER W. B., I.; ROUSSEV, I. I.; TÓTH, G.; GOMBOSI, T. I. Numerical investigation of the homologous coronal mass ejection events from active region 9236. **The Astrophysical Journal**, v. 659, n. 1, p. 788–800, apr. 2007. 25, 28, 33, 38, 57

LUGAZ, N.; MANCHESTER W.B., I.; GOMBOSI, T. The evolution of coronal mass ejection density structures. **The Astrophysical Journal**, v. 627, n. 2, p. 1019–1030, jul. 2005a. 25, 28, 29, 33

LYON, J. G. The solar wind-magnetosphere-ionosphere system. **Science**, v. 288, p. 1987–1991, jun. 2000. 20

LYON, J. G.; FEDDER, J. A.; HUBA, J. D. The effect of different resistivity models on magnetotail dynamics. **Journal of Geophysical Research**, v. 91, p. 8057–8064, jul. 1986. 27

MANCHESTER, W. Buoyant disruption of magnetic arcades with self-induced shearing. **Journal of Geophysical Research**, v. 108, n. A4, p. v, apr. 2003. 25, 28

MANCHESTER, W.; GOMBOSI, T.; ROUSSEV, I.; ZEEUW, D. L. D.; SOKOLOV, I.; POWELL, K.; TÓTH, G.; OPHER, M. Three-dimensional MHD simulation of a flux rope driven CME. **Journal of Geophysical Research**, v. 109, n. A1, jan. 2004a. 24, 25, 28, 29, 33, 35, 36, 41, 55, 72

MANCHESTER, W.; GOMBOSI, T.; ROUSSEV, I.; RIDLEY, A.; ZEEUW, D. D.; SOKOLOV, I.; POWELL, K.; TÓTH, G. Modeling a space weather event from the Sun to the Earth: CME generation and interplanetary propagation. **Journal of Geophysical Research**, v. 109, n. A2, feb. 2004b. 24, 25, 27, 28, 33

MANCHESTER, W. B.; GOMBOSI, T.; ZEEUW D. L.AND SOKOLOV, I. V. D.; ROUSSEV, I.; POWELL, K. G.; KÓTA, J.; TÓTH, G.; ZURBUCHEN, T. H. Coronal mass ejection shock and sheath structures relevant to particle acceleration. **The Astrophysical Journal**, v. 622, n. 2, p. 1225–1239, apr. 2005. 25, 28, 31, 33, 55, 56, 59, 65, 71, 72

MANCHESTER, W. I. Solar atmospheric dynamic coupling due to shear motions driven by the Lorentz force. **The Astrophysical Journal**, v. 666, n. 1, p. 532–540, sept. 2007. 32

MANCUSO, S.; RAYMOND, J. C.; KOHL, J.; KO, Y.-K.; UZZO, M.; WU, R. UVCs/SOHO observations of a CME-driven shock: consequences on ion heating mechanisms behind a coronal shock. **Astronomy and Astrophysics**, v. 383, p. 267–274, jan. 2002. 56

MCCOMAS, D. J.; BAME, S. J.; BARRACLOUGH, B. L.; FELDMAN, W. C.; FUNSTEN, H. O.; GOSLING, J. T.; RILEY, P.; SKOUG, R.; BALOGH, A.; FORSYTH, R.; GOLDSTEIN, B. E.; NEUGEBAUER, M. Ulysses' return to the slow solar wind. **Geophysical Research Letters**, v. 25, n. 1, p. 1–4, 1998. 21

ODSTRCIL, D.; DRYER, M.; SMITH, Z. Propagation of an interplanetary shock along the heliospheric plasma sheet. **Journal of Geophysical Research**, v. 101, n. A9, p. 19973–19986, sep. 1996. 55

ODSTRCIL, D.; LINKER, J. A.; LIONELLO, R.; MIKIĆ, Z.; RILEY, P.; PIZZO, V. J.; LUHMANN, J. G. Merging of coronal and heliospheric numerical two-dimensional MHD models. **Journal of Geophysical Research**, v. 107, n. A12, dec. 2002. 24, 27

ODSTRCIL, D.; PIZZO, V. J. Three-dimensional propagation of CMEs in a structured solar wind flow: 1. CME launched within the streamer belt. **Journal of Geophysical Research**, v. 104, n. A1, p. 483–492, jan. 1999. 27

_____. Three-dimensional propagation of coronal mass ejections in a structured solar wind flow 2. CME launched adjacent to the streamer belt. **Journal of Geophysical Research**, v. 104, n. A1, p. 493–504, jan. 1999. 27

OGINO, T.; WALKER, R. J. A magnetohydrodynamic simulation of the bifurcation of tail lobes during intervals with a northward interplanetary magnetic field. **Geophysical Research Letters**, v. 11, p. 1018–1021, oct. 1984. 27

PARKS, G. K. **Physics of space plasmas**: an introduction. California: Addison-Wesley Publishing Company, 1991. 538 p. 21, 59

PIZZO, V. J. The evolution of corotating stream fronts near the ecliptic plane in the inner solar system. II - three-dimensional tilted-dipole fronts. **Journal of Geophysical Research**, v. 96, n. 1, p. 5405–5420, apr. 1991. 27

POWELL, K. G.; ROE, P. L.; LINDE, T. J.; GOMBOSI, T. I.; ZEEUW, D. L. de. Solution-adaptive upwind scheme for ideal magnetohydrodynamics. **Journal of Computational Physics**, v. 154, p. 284–309, sept. 1999. 29, 31

RAYMOND, J. C.; THOMPSON, B. J.; CYR, O. C. S.; GOPALSWAMY, N.; KAHLER, S.; KAISER, M.; LARA, A.; CIARAVELLA, A.; ROMOLI, M.; O'NEAL, R. SOHO and radio observations of a CME shock wave. **Geophysical Research Letters**, v. 27, n. 10, p. 1439–1442, may 2000. 56

REAMES, D. V. Magnetic topology of impulsive and gradual solar energetic particle events. **The Astrophysical Journal**, v. 571, n. 1, p. L63–L66, may 2002. 65

RICHARDSON, J. D.; LIU, Y. A comparison of magnetosheaths, ICME sheaths, and the heliosheath. In: TURBULENCE AND NONLINEAR PROCESSES IN ASTROPHYSICAL PLASMAS, 6th ANNUAL INTERNATIONAL ASTROPHYSICS CONFERENCE, 6., 2007, Oahu, United States of America. **Proceedings...** [S.l.]: AIP Conference Proceedings, 2007. v. 932, p. 387–392. 62

RIDLEY A. J.AND RICHMOND, A. D.; GOMBOSI, T. I.; ZEEUW, D. L. D.; CLAUER, C. R. Ionospheric control of the magnetospheric configuration: thermospheric neutral winds. **Journal of Geophysical Research**, v. 108, n. A8, aug. 2003. 27

RILEY, P.; LINKER, J. A.; MIKIC, Z.; LIONELLO, R.; LEDVINA, S. A.; LUHMANN, J. G. A comparison between global solar magnetohydrodynamic and potential field source surface model results. **The Astrophysical Journal**, v. 653, n. 2, p. 1510–1516, dec. 2006. 44, 45, 46

ROUSSEV, I. I.; FORBES, T. G.; GOMBOSI, T. I.; SOKOLOV, I. V.; DEZEEUW, D. L.; BIRN, J. A three-dimensional flux rope model for coronal mass ejections based on a loss of equilibrium. **The Astrophysical Journal**, v. 588, n. 1, p. L45–L48, may 2003a. 24, 25, 28, 32, 33, 38, 39, 41

ROUSSEV, I. I.; GOMBOSI, T. I.; SOKOLOV, I. V.; VELLI, M.; MANCHESTER, W. B. A three-dimensional model of the solar wind incorporating solar magnetogram observations. **The Astrophysical Journal**, v. 595, p. L57–L61, sep. 2003b. 31, 41

ROUSSEV, I. I.; LUGAZ, N.; SOKOLOV, I. V. New physical insight on the changes in magnetic topology during coronal mass ejections: case studies for the 2002 April 21 and August 24 events. **The Astrophysical Journal**, v. 668, n. 1, p. L87–L90, oct. 2007. 32

ROUSSEV, I. I.; SOKOLOV, I. V.; FORBES, T. G.; GOMBOSI, T. I.; LEE, M. A.; SAKAI, J. I. A numerical model of a coronal mass ejection: shock development with implications for the acceleration of GeV protons. **The Astrophysical Journal**, v. 605, n. 1, p. L73–L76, apr. 2004. 24, 25, 28, 33, 44, 56

SCHATTEN, K. H. Current sheet magnetic model for the solar corona. **Cosmic Electrodynamics**, v. 2, p. 232–245, 1971. 46

SCHATTEN, K. H.; WILCOX, J. M.; NESS, N. F. A model of interplanetary and coronal magnetic fields. **Solar Physics**, v. 6, n. 3, p. 442–455, mar. 1969. 44, 46

SCHWENN, R. An essay on terminology, myths and known facts: Solar transient - flare - CME - driver gas - piston - BDE - magnetic cloud - shock wave - geomagnetic storm. In: SOLAR AND INTERPLANETARY TRANSIENTS, IAU COLLOQUIUM, 154., 1995, Pune, India. **Proceedings...** [S.l.]: Astrophysics and Space Science, 1996. p. 187–193. 23

SIME, D. G.; HUNDHAUSEN, A. J. The coronal mass ejection of July 6, 1980 - a candidate for interpretation as a coronal shock wave. **Journal of Geophysical Research**, v. 92, p. 1049–1055, feb. 1987. 56

SOHO (ESA and NASA). 2004. CME as seen by LASCO. Available at: <http://www.esa.int/esaSC/Pr_13_2004_s_en.html>. Acess in: February 22, 2009. 53

_____. 2006. "Lightbulb" CME. Available at: <http://sohowww.nascom.nasa.gov/gallery/images/las02.html>. Acess in: January 20, 2009. 23

_____. 2007. MDI synoptic chart for Carrington rotation 1922. Available at: <http://soi.stanford.edu/magnetic/synoptic/carrot/M/1922/synop_Mr_45E.1922.gif>. Acess in: February 26, 2009. 45

TITOV, V. S.; DÉMOULIN, P. Basic topology of twisted magnetic configuration in solar flares. **Astronomy & Astrophysics**, v. 351, p. 707 – 720, nov. 1999. 17, 25, 28, 32, 33, 36, 37, 38, 48

TÓTH, G.; SOKOLOV, I. V.; GOMBOSI, T. I.; CHESNEY, D. R.; CLAUER, C. R.; ZEEUW, D. L. D.; HANSEN, K. C.; KANE, K. J.; MANCHESTER, W. B.; OEHMKE, R. C.; POWELL, K. G.; RIDLEY, A. J.; ROUSSEV, I. I.; STOUT, Q. F.; VOLBERG, O.; WOLF, R. A.; SAZYKIN, S.; CHAN, A.; YU, B.; KÓTA, J. Space weather modeling framework: a new tool for the space science community. **Journal of Geophysical Research**, v. 111, n. A12, dec. 2005. 28, 30

TOTTEN, T. L.; FREEMAN, J. W.; ARYA, S. Application of the empirically derived polytropic index for the solar wind to models of solar wind propagation. **Journal of Geophysical Research**, v. 101, n. A7, p. 15629–15636, jul. 1996. 44, 46

TSURUTANI, B.; WU, S. T.; ZHANG, T. X.; DRYER, M. Coronal mass ejection (CME)-induced shock formation, propagation and some temporally and spatially developing shock parameters relevant to particle energization. **Astronomy and Astrophysics**, v. 412, p. 293–304, dec. 2003. 55

TSURUTANI, B. T.; GONZALEZ, W. D. Magnetic storms. In: **From the Sun, auroras, magnetic storms, solar flares, cosmic rays**. Washington, DC: American Geophysical Union, 1998. p. 77. 23

TSURUTANI, B. T.; RUSSELL, C. T.; KING, J. H.; ZWICKL, R. D.; LIN, R. P. A kinky heliospheric current sheet - cause of CDAW-6 substorms. **Geophysical Research Letters**, v. 11, p. 339–342, apr. 1984. 60

TSURUTANI, B. T.; SMITH, E. J.; GONZALEZ, W. D.; TANG, F.; AKASOFU, S. I. Origin of interplanetary southward magnetic fields responsible for major magnetic storms near solar maximum (1978-1979). **Journal of Geophysical Research**, v. 93, p. 8519–8531, 1988. 61

TYLKA, A. J. New insights on solar energetic particles from Wind and ACE. **Journal of Geophysical Research**, v. 106, n. A11, p. 25333–25352, nov. 2001. 65

USMANOV, A. V. Numerical 3-D time-dependent MHD model of the solar wind. **Space Science Reviews**, v. 72, n. 1-2, p. 121–124, apr. 1995. 27

USMANOV, A. V.; GOLDSTEIN, M. L. A tilted-dipole MHD model of the solar corona and solar wind. **Journal of Geophysical Research**, v. 108, n. A9, p. SSH 1–1, sep. 2003. 43

VOURLIDAS, A.; BUZASI, D.; HOWARD, R. A.; ESFANDIARI, E. Mass and energy properties of LASCO CMEs. In: SOLAR VARIABILITY: FROM THE CORE TO OUTER FRONTIERS. THE 10th EUROPEAN SOLAR PHYSICS MEETING. 10., 2002. Prague, Czech Republic. **Proceedings...** Noordwijk: ESA Publications Division, 2002, p. 91–94. ISBN 92-9092-816-6. 23

WANG, R.; WANG, J. Spectra and solar energetic protons over 20 GeV in bastille day event. **Astroparticle Physics**, v. 25, n. 1, p. 41–46, feb. 2006. 24

WANG, Y. M.; WANG, S.; YE, P. Z. Multiple magnetic clouds in interplanetary space. **Solar Physics**, v. 211, n. 1, p. 333–344, dec. 2002. 27

WEBB, D. F.; HOWARD, R. A. The solar cycle variation of coronal mass ejections and the solar wind mass flux. **Journal of Geophysical Research**, v. 99, n. A3, p. 4201–4220, mar. 1994. 24

WU, S. T.; ANDREWS, M. D.; PLUNKETT, S. P. Numerical magnetohydrodynamic (MHD) modeling of coronal mass ejections (CMEs). **Space Science Reviews**, v. 95, n. 1/2, p. 191–213, jan. 2001. 24

WU, S. T.; GUO, W. P.; MICHELS, D. J.; BURLAGA, L. F. MHD description of the dynamical relationships between a flux rope, streamer, coronal mass ejection, and magnetic cloud: an analysis of the January 1997 Sun-Earth connection event. **Journal of Geophysical Research**, v. 104, n. A7, p. 14789–14802, sept. 1999. 25, 27, 28

WU, S. T.; GUO, W. P.; PLUNKETT, S. P.; SCHMIEDER, B.; SIMNETT, G. M. Coronal mass ejections (CMEs) initiation: models and observations. **Journal of Atmospheric and Solar-Terrestrial Physics**, v. 62, n. 16, p. 1489–1498, nov. 2000. 28

ZHANG, J.; DERE, K. P.; HOWARD, R. A.; VOURLIDAS, A. A study of the kinematic evolution of coronal mass ejections. **The Astrophysical Journal**, v. 604, n. 1, p. 420–432, mar. 2004. 53, 57, 58

ZHANG, J.; LIEMOHN, M. W.; ZEEUW, D. L. D.; BOROVSKY, J. E.; RIDLEY, A. J.; TOTH, G.; SAZYKIN, S.; THOMSEN, M. F.; KOZYRA, J. U.; GOMBOSI, T. I.; WOLF, R. A. Understanding storm-time ring current development through data-model comparisons of a moderate storm. **Journal of Geophysical Research**, v. 112, n. A4, apr. 2007. 27

ZHANG, J.; POOMVISES, W.; RICHARDSON, I. G. Sizes and relative geoeffectiveness of interplanetary coronal mass ejections and the preceding shock sheaths during intense storms in 1996-2005. **Geophysical Research Letters**, v. 35, n. 2, jan. 2008. 61

Livros Grátis

(http://www.livrosgratis.com.br)

Milhares de Livros para Download:

Baixar livros de Literatura
Baixar livros de Literatura de Cordel
Baixar livros de Literatura Infantil
Baixar livros de Matemática
Baixar livros de Medicina
Baixar livros de Medicina Veterinária
Baixar livros de Meio Ambiente
Baixar livros de Meteorologia
Baixar Monografias e TCC
Baixar livros Multidisciplinar
Baixar livros de Música
Baixar livros de Psicologia
Baixar livros de Química
Baixar livros de Saúde Coletiva
Baixar livros de Serviço Social
Baixar livros de Sociologia
Baixar livros de Teologia
Baixar livros de Trabalho
Baixar livros de Turismo